

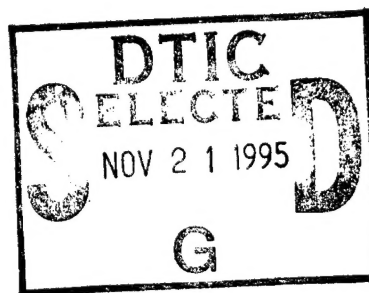
IMPACT OF AEROSOL FORWARD SCATTERING ON THE ABL SYSTEM

David R. Longtin
Michael G. Cheifetz

SPARTA, Inc.
24 Hartwell Avenue
Lexington, MA 02173

20 December 1994

Scientific Report No. 10



Approved for public release; distribution unlimited



PHILLIPS LABORATORY
Directorate of Geophysics
AIR FORCE MATERIEL COMMAND
HANSCOM AFB, MA 01731-3010

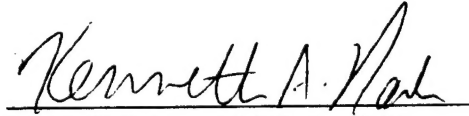
19951115 099

DTIC QUALITY INSPECTED 5

"This technical report has been reviewed and is approved for publication "



ROBERT R. BELAND
Contract Manager



KENNETH A. NASH, Lt Col
Branch Chief



ROGER A. VAN TASSEL
Division Director

This report has been reviewed by the ESC Public Affairs Office (PA) and is releasable to the National Technical Information Service (NTIS).

Qualified requestors may obtain additional copies from the Defense Technical Information Center (DTIC). All others should apply to the National Technical Information Service (NTIS).

If your address has changed, if you wish to be removed from the mailing list, or if the addressee is no longer employed by your organization, please notify PL/IM, 29 Randolph Road, Hanscom AFB, MA 01730-3010. This will assist us in maintaining a current mailing list.

Do not return copies of this report unless contractual obligations or notices on a specific document requires that it be returned.

REPORT DOCUMENTATION PAGE			Form Approved OMB No. 0704-0188	
Public reporting burden for this collection of information is estimated to average 1 hour per response, including the time for reviewing instructions, searching existing data sources, gathering and maintaining the data needed, and completing and reviewing the collection of information. Send comments regarding this burden estimate or any other aspect of this collection of information, including suggestions for reducing this burden, to Washington Headquarters Services, Directorate for Information Operations and Reports, 1215 Jefferson Davis Highway, Suite 1204, Arlington, VA 22202-4302, and to the Office of Management and Budget, Paperwork Reduction Project (0704-0188), Washington, DC 20503.				
1. AGENCY USE ONLY (Leave blank)		2. REPORT DATE 20 December 1994		3. REPORT TYPE AND DATES COVERED Scientific Report No. 10
4. TITLE AND SUBTITLE Impact of Aerosol Forward Scattering on the ABL System			5. FUNDING NUMBERS PE 35160F PR 7670 TA 15 WUBB F19628-91-C-0093	
6. AUTHOR(S) David R. Longtin and Michael G. Cheifetz				
7. PERFORMING ORGANIZATION NAME(S) AND ADDRESS(ES) SPARTA, Inc. 24 Hartwell Avenue Lexington, MA 02173			8. PERFORMING ORGANIZATION REPORT NUMBER LTR94-003	
9. SPONSORING / MONITORING AGENCY NAME(S) AND ADDRESS(ES) Phillips Laboratory 29 Randolph Road Hanscom Air Force Base, MA 01731-3010 Contract Manager: Robert Beland/GPOA			10. SPONSORING / MONITORING AGENCY REPORT NUMBER PL-TR-94-2312	
11. SUPPLEMENTARY NOTES				
12a. DISTRIBUTION / AVAILABILITY STATEMENT Approved for Public Release; Distribution Unlimited.			12b. DISTRIBUTION CODE	
13. ABSTRACT (Maximum 200 words) The AirBorne Laser (ABL) theater missile defense system involves the delivery of large amounts of highly focused energy across long, nearly horizontal paths in the upper troposphere and stratosphere. The current study addresses whether high amounts of aerosol forward scattering may impact ABL performance. The current study asserts that aerosol forward scattering effects are minimal for the ABL system and cannot account for the starlight scintillation behavior as measured by aircraft at ABL altitudes. Using appropriate scattering theories and numerical simulation techniques, the analysis considered possible contributions from the single scattering diffraction peak as well as multiple scattering near the optical axis. It was found that the characteristic scattering angles for background stratospheric aerosols and thin cirrus are too large, especially when compared with the transmitter divergence angles of the high energy laser and the tracking laser which are on the order of microradians to milliradians. Scattering energy is directed well away from the optical axis and, therefore, the energy received near on-axis effectively equals the energy transmitted through the atmosphere. On-axis forward scattering effects become important for background stratospheric aerosols and thin cirrus only when scattering optical depths are on the order of 10 or greater.				
14. SUBJECT TERMS Airborne Laser System (ABL), Aerosol Forward Scattering, Laser Propagation, Aerosol Modulation Transfer Function (MTF), Scattering Optical Depth, Thin Cirrus, Background Stratospheric Aerosol			15. NUMBER OF PAGES 46	
			16. PRICE CODE	
17. SECURITY CLASSIFICATION OF REPORT Unclassified	18. SECURITY CLASSIFICATION OF THIS PAGE Unclassified	19. SECURITY CLASSIFICATION OF ABSTRACT Unclassified	20. LIMITATION OF ABSTRACT SAR	

Accession For	
NTIS CRA&I	<input checked="" type="checkbox"/>
DTIC TAB	<input type="checkbox"/>
Unannounced	<input type="checkbox"/>
Justification	
By	
Distribution /	
Availability Codes	
Dist	Avail and / or Special
A-1	

Table of Contents

1 INTRODUCTION	1
1.1 Background and Purpose of This Study	1
1.2 Organization of the Report	2
2 NUMERICAL ASSESSMENT OF AEROSOL FORWARD SCATTERING	3
2.1 General Aerosol Characteristics for ABL Engagements	3
2.2 Single Scattering Effects	4
2.2.1 Aerosol RMS Scattering Angles	4
2.2.2 Contributions from the Aerosol Diffraction Peak	5
2.3 Multiple Forward Scattering Effects	7
2.3.1 Aerosol Modulation Transfer Function	7
2.3.2 Angular Extent of Aerosol Multiple Forward Scattering	9
2.3.3 Aperture Effects	12
2.3.4 Beam Spread Pattern from Aerosol Multiple Forward Scattering	16
2.4 Impact of Inhomogeneous Scattering on the Beam Spread Pattern	18
3 LITERATURE SURVEY	21
3.1 Experiment Summary	22
3.2 Comparisons Against Current Results	23
4 SUMMARY AND POSSIBLE ENHANCEMENTS	24
4.1 Summary	24
4.2 Possible Enhancements	24
REFERENCES	26

APPENDIX A	28
A.1 Program <i>l7abl</i>	28
A.2 Program <i>msct</i>	29
A.3 Program <i>iradapx</i>	29
A.4 Program <i>irad</i>	30

List of Figures

1. Apparent to Actual Transmittance Ratio for Different Particle Sizes and ABL Field-of-View Conditions	7
2. Conceptual Form of the Aerosol Modulation Transfer Function, M_{aer}	9
3. Multiple Scattering Component of the Aerosol Modulation Transfer Function (M_{sct}) for Background Stratospheric Aerosols and Cirrus	10
4. Transverse Coherence Length (ρ_a) as a Function of Scattering Optical Depth at Visible Wavelengths	10
5. Transverse Coherence Length (ρ_a) as a Function of Scattering Optical Depth at ABL Wavelengths	11
6. Scattering Divergence Half-Angle as a Function of Scattering Optical Depth at Visible Wavelengths	11
7. Scattering Divergence Half-Angle as a Function of Scattering Optical Depth at ABL Wavelengths	12
8. Ratio of the Visible Peak Diffraction-Limited Spot Intensity to Peak Multiple Scatter Intensity as a Function of Scattering Optical Depth for a 10 cm Diameter Receiver	13
9. Ratio of the ABL Peak Diffraction-Limited Spot Intensity to Peak Multiple Scatter Intensity as a Function of Scattering Optical Depth for a 10 cm ABL Diameter	14
10. Ratio of the Visible Peak Diffraction-Limited Spot Intensity to Peak Multiple Scatter Intensity as a Function of Scattering Optical Depth for a 1 cm Diameter Receiver	14
11. Ratio of the ABL Peak Diffraction-Limited Spot Intensity to Peak Multiple Scatter Intensity as a Function of Scattering Optical Depth for a 50 cm ABL Diameter	15
12. Scattering Optical Depth Required for Equal Peak Intensities Due to Incoherent Scattering and Diffraction Effects for a Monodisperse Aerosol	16
13. Beam Spread Pattern as a Function of Scattering Optical Depth	18
14. Beam Spread Pattern For Different Aerosol Asymmetry Parameters	19
15. Scattering Geometry of a "Narrow" Beam As It Encounters a Thin Diffuse Scattering Layer	20
16. Half-Angle Beam Spread Due to a Thin Scattering Layer as a Function of Transmitter-to-Layer Distance	21

A-1. Sample Input File for <i>l7abl</i>	29
A-2. Sample Output File from <i>l7abl</i>	31
A-3. Sample Output File from <i>msct</i>	34
A-4. Sample Output File from <i>iradapx</i>	36
A-5. Sample Output File from <i>irad</i>	37

List of Tables

1. Physical Properties of Possible Aerosols in an ABL Engagement	4
2. Scattering Optical Depths at Visible and ABL Wavelengths for Background Stratospheric Aerosols (BS) and Thin Cirrus (CI)	5
3. RMS Scattering Angles for Background Stratospheric Aerosols and Thin Cirrus	5
4. Size Parameters and Forward Scattering Correction Factors for Different Aerosol Types	6
5. Comparison of the On-Axis Transmitted Intensity Against the Calculated On-Axis Intensity as a Function of Scattering Optical Depth	19
6. Aerosol Forward Scattering Effects on a Point Source During Different Aerosol Events as Reported by Bissonnette	22
7. Appearance of a Light Bulb As Viewed Through a Scattering Medium from Linskens and Bohren	23
A-1. Format of the Input File for <i>l7abl</i>	28
A-2. Input Parameters for <i>irad</i>	36

IMPACT OF AEROSOL FORWARD SCATTERING ON THE ABL SYSTEM

1 INTRODUCTION

1.1 Background and Purpose of This Study

The AirBorne Laser (ABL) theater missile defense system involves the delivery of large amounts of highly focused energy across long, nearly horizontal paths in the upper troposphere and stratosphere. As conceived, the system is mounted on an aircraft at an altitude of 12.5 km (41,000 ft). A tracking laser ($\sim 1.06 \mu\text{m}$) monitors the missile trajectory and the reflected laser energy from the missile is used as an adaptive optics beacon. A high energy $1.32 \mu\text{m}$ Chemical Oxygen Iodine Laser (COIL) is then used to engage the missile.

To date, a number of studies have dwelled on the impact of atmospheric aerosols on ABL performance.¹ The main focus of these efforts has been to determine what optical depths will exist at ABL altitudes and engagement scenarios and how this will affect the propagation of the high power laser beam to target. At sufficiently large optical depths, this can drastically reduce the beam transmission and coherence, thus rendering the system inoperable. Recently however, it has been speculated that high amounts of aerosol forward scattering may impact ABL performance. That is, provided the aerosol is sufficiently large, it is possible for scattered energy to remain in a particular line-of-sight or (re)enter it after encountering subsequent

¹ W.J. Schafer Associates (Coord.) (1993) *Airborne Laser Workshop on Cirrus and Volcanic Aerosols*, Meeting held at W.J. Schafer Associates, Alexandria, VA.

scattering events. For the ABL tracking lidar, the net effect could be to increase the amount of image blurring and adversely effect adaptive optics. For the high energy COIL, aerosol forward scattering could restrict the beam broadening and add (incoherent) energy upon the missile.

The impetus to investigate aerosol forward scattering effects comes from measurements of starlight scintillation by aircraft at ABL altitudes.² These measurements indicate that for elevation angles near zero, the variance of stellar intensity becomes abnormally constant for a span of several days regardless of geographical location. Although Herrmann and Zollars³ attribute this behavior to atmospheric dispersion of the (broadband) starlight and the resulting refractive anisoplanatism, it is not certain if image blurring due to aerosol forward scattering can also cause the same behavior.

The current study asserts that aerosol forward scattering effects are minimal for the ABL system. This assertion includes contributions from the single scattering diffraction peak and multiple scattering effects. For multiple scattering, it is important to recognize the ~70% transmission criterion for ABL operation, which converts to optical depths of 0.25 or less.⁴ Typically, a multiple scattering medium requires scattering optical depths of 0.2,⁵ at least, which is a borderline situation for the ABL system to operate. However, this study will show that for the particle types and sizes to be present at ABL altitudes, scattering optical depths must be much greater (exceeding 10) for multiple forward scattering effects to be important.

1.2 Organization of the Report

Using techniques in the scientific literature, Chapter 2 numerically evaluates the impact of aerosol forward scattering on the ABL system. Chapter 3 briefly describes work by other researchers in the scientific literature that is relevant to this study. Chapter 4 presents a summary and conclusions. Finally, Appendix A documents the computer programs that were developed in this study.

² Kramer, M.A. (1993) "Stellar Scintillometry Flight aboard HALO," Phillips Laboratory, Albuquerque, NM, PL-TR-93-1004.

³ Herrmann, J. and Zollars, B.G. (1994) "Interpretation of Airborne Stellar Scintillation Measurements Made by the Phillips Laboratory," Massachusetts Institute of Technology Lincoln Laboratory, Lexington, MA, Memo No. 94PM-ACP-0030.

⁴ Harada, L.K., Leslie, D.H., and Salazar, M. (1994) "Atmospheric transmission analysis for airborne laser applications," *Laser Beam Propagation and Control*, from Proceedings SPIE 2120, Los Angeles, CA.

⁵ Sassen, K. (1991) Corona-producing cirrus cloud properties derived from polarization lidar and photographic analysis, *Applied Optics*, **30**:3421-3428.

2 NUMERICAL ASSESSMENT OF AEROSOL FORWARD SCATTERING

Numerical techniques in the scientific literature can be used to evaluate the potential impact of aerosol forward scattering on the ABL system. Although computationally intensive, Monte Carlo simulations and discrete-ordinate solutions to theoretical radiative transfer are available. Bissonnette⁶ developed a general purpose propagation model for narrow light beams in which the lateral transport of scattered intensity is represented by a diffusion process.

The current study addresses aerosol single and multiple scattering processes separately. For single scattering, the Mill and Shettle⁷ formulation is applied. For multiple scattering, the concepts and equations given in Lutomirski⁸ and the IR/EO Systems Handbook⁹ are used. To isolate the potential impact of aerosol forward scattering, the effects of turbulence, aerosol absorption, and molecular absorption are not included.

2.1 General Aerosol Characteristics for ABL Engagements

Typical ABL engagements will encounter aerosols in the uppermost troposphere, stratospheric aerosols, volcanic aerosols, and/or cirrus. The physical characteristics of the aforementioned aerosols are summarized in Table 1. Background aerosols in the upper troposphere and stratosphere generally have radii less than 1 μm . Immediately following strong eruptions, fresh volcanic aerosols occasionally have particles with radii between 10 and 20 μm , but they quickly settle out so aged volcanic aerosols generally have radii of less than 1 μm . Ice crystal lengths in thin cirrus are usually less than 50 μm .¹⁰ Although extreme natural variability exists, thicker cirriform clouds are generally composed of ice crystals smaller than 250 μm (in length) with isolated larger particles.¹¹ Because the ice crystal shapes are plates, columns, and needles, which may or may not be preferably oriented, Mie theory calculations only approximate

⁶ Bissonnette, L.R. (1988) Multiscattering model for propagation of narrow light beams in aerosol media, *Applied Optics*, **27**: 2478-2484.

⁷ Mill, J.D. and Shettle, E.P. (1983) "A Preliminary LOWTRAN Snow Model," Air Force Geophysics Laboratory, Hanscom AFB, MA, AFGL-TR-83-1048, ADA129826.

⁸ Lutomirski, R.L. (1978) Atmospheric degradation of electrooptical system performance, *Applied Optics*, **17**: 3915-3921.

⁹ Accetta, J.S., and Shumaker, D.L. (Chief Eds.) (1993) *The Infrared and Electro-Optical Systems Handbook, Volume 2, Atmospheric Propagation of Radiation*, F.G. Smith (Ed.), Chapter 1 by M.E. Thomas and D.D. Duncan, ERIM Infrared Information Analysis Center and SPIE Optical Engineering Press (Copubl.), Ann Arbor, Michigan and Bellingham, Washington, p. 123.

¹⁰ Grantham, D.D., *et al.* (1985) "Water Vapor, Precipitation, Clouds, and Fog," Chapter 16 in *Handbook of Geophysics and the Space Environment*, A.S. Jursa Scientific Editor, Air Force Geophysics Laboratory, Hanscom AFB, MA, AFGL-TR-85-0315, ADA167000.

¹¹ Sassen, K., Knight, N.C., Takano, Y., and Heymsfield, A.J. (1994) Effects of ice-crystal structure on halo formation: cirrus cloud experimental and ray-tracing modeling studies, *Applied Optics*, **33**:4590-4601.

the scattering phase function. The current study focuses on background stratospheric aerosols and thin cirrus because they are most likely to be present in ABL engagements plus they exhibit very different forward scattering behavior due to their sizes.

Table 1. Physical Properties of Possible Aerosols in an ABL Engagement

AEROSOL TYPE	COMPOSITION	GENERAL SIZE	GENERAL SHAPE
Upper tropospheric	Dust/water soluble mixture	Submicron	Spherical
Background stratospheric	Sulfuric acid solution	Submicron	Spherical
Volcanic	Volcanic dust/ash	10-20 μm after eruptions	Irregular
Thin cirrus	Ice	Generally < 50 μm	Plates, columns, needles

Table 2 shows representative aerosol scattering optical depths, τ_{scat} , at visible and ABL wavelengths. The scattering optical depths for background stratospheric aerosols were obtained from LOWTRAN7¹² using a moderate stratospheric loading profile. The moderate loading profiles for Midlatitude Spring/Summer and Fall/Winter conditions gave similar scattering optical depths. The cirrus scattering optical depths were derived from a cirrus transmission analysis by Koenig *et al.*¹³ A range of thin cirrus scattering optical depths is shown in Table 2 because cirrus extinction coefficients are inherently variable and because their impact depends on the cloud altitude and thickness. Effectively, the upper limits in Table 2 correspond to the greatest transmission reduction as reported by Koenig *et al.*

2.2 Single Scattering Effects

2.2.1 Aerosol RMS Scattering Angles

In general, the amount of aerosol forward scattering depends on the aerosol shape and size, as well as scattering optical depth. For a single scattering medium, the degree of scattering in the forward direction by an aerosol can be characterized by the RMS scattering angle which is defined as

$$\theta_{rms} = \langle \theta^2 \rangle = \sqrt{2\pi \int_0^\pi d\theta P(\theta) \theta^2 \sin \theta}. \quad (1)$$

¹² Kneizys, F.X., Shettle, E.P., Abreu, L.W., Chetwynd, J.H., Anderson, G.P., Gallery, W.O., Selby, J.E.A., and Clough, S.A. (1988) *Users Guide to LOWTRAN7*, Air Force Geophysics Laboratory, Hanscom, AFB, Massachusetts, AFGL-TR-88-0177, ADA206773.

¹³ Koenig, G.G., Longtin, D.R., and Hummel, J.R. (1993) "A Study of the Impact of Cirrus Clouds on High Altitude, Long Horizontal Path Laser Transmission," Phillips Laboratory, Hanscom AFB, MA, PL-TR-93-2263, ADA278563.

Table 2. Scattering Optical Depths at Visible and ABL Wavelengths for Background Stratospheric Aerosols (BS) and Thin Cirrus (CI). The upper limits for cirrus assume an $0.55 \mu\text{m}$ extinction coefficient of 0.03 km^{-1} which is consistent with the thin cirrus model in LOWTRAN7. The aircraft altitude is 12.5 km

MISSILE ALTITUDE (km)	τ_{sct} (BS) Visible	τ_{sct} (BS) ABL	τ_{sct} (CI) ABL
15.3	0.80	0.15	0-3.60
37.1	0.60	0.12	0-1.09
50.3	0.56	0.12	0-1.03
92.1	0.26	0.05	0-0.38

where $P(\theta)$ is the aerosol phase function at the scattering angle θ . Using aerosol phase functions from LOWTRAN7, Table 3 shows the RMS scattering angle for background stratospheric aerosols and thin cirrus. (The thin cirrus values are approximate because the particles are nonspherical with some preferred orientation.) Due to the larger particles, thin cirrus have much narrower RMS scattering angles than background stratospheric aerosols. However, the RMS scattering angles for both aerosols are on the order of tens of degrees which indicates that most scattered energy is towards wide angles and cannot impact the ABL optics.

Table 3. RMS Scattering Angles for Background Stratospheric Aerosols and Thin Cirrus

AEROSOL TYPE	RMS SCATTERING ANGLE	
	Visible	ABL
Background Stratospheric	51.6° (0.901 rad)	65.3° (1.140 rad)
Thin Cirrus	30.2° (0.527 rad)	26.4° (0.461 rad)

2.2.2 Contributions from the Aerosol Diffraction Peak

Single scattered radiation from atmospheric aerosols is characterized by a diffraction peak in the forward direction. The shape and magnitude of the peak depend on the particle size, shape, and orientation. If the peak is large and narrow, scattered energy can remain within a transmissometer field-of-view resulting in an apparent (*i.e.*, measured) transmission that exceeds the true transmission. For the high energy COIL, the net effect would be a direction of incoherent energy to the missile. Given that the ABL system will usually operate under single scattering conditions, an unqualified assessment of particle diffraction effects is justified.

Although the Mill and Shettle model was developed to remove forward scattering effects from transmissometer data, it can be used to estimate particle diffraction effects within the (finite) field-of-view conditions of an ABL engagement. The measured transmission, T_m , and the true transmission, T , are related as

$$T_m = T(1 - D' \ln T) \quad (2)$$

where the correction term D' equals

$$D' = x^2 \int_0^{\Psi} \int_0^{\Theta} \left\{ \frac{J_1(x \sin(\Theta' + \Psi'))}{x \sin(\Theta' + \Psi')} \right\}^2 F(\Theta') d\Theta' d\Psi' \quad (3)$$

In Eq. 3, Θ is the half-angle of the receiver field-of-view (FOV), Ψ is the source half-angle, $F(\Theta')$ is the detector response, x is the particle size parameter ($=2\pi r/\lambda$), r is the particle radius, λ is the wavelength, and J_1 is the Bessel function of the first kind and first order. The formulation assumes multiple scattering is negligible, Θ and Ψ are less than 5° , and the aerosol phase function can be represented by Fraunhofer diffraction. Also, it is assumed that the aerosol can be represented by an effective scattering radius.

Ratios of T_m/T were obtained for particle sizes that characterize background stratospheric aerosols, thin cirrus, and cirrus. For the high energy COIL, the beam divergence (*i.e.*, the source FOV) and the laser spot size on the missile (*i.e.*, the receiver FOV) are on the order of microradians. For the ABL tracking lidar, the imaging receiver FOV is set to one milliradian and the source represents scattered energy off the missile. For the purposes of this application, it is sufficient to treat the source FOV as being much larger than the receiver FOV. A flat receiver response ($F(\Theta)=1$) is assumed for simplicity. Table 4 summarizes other parameters for this analysis.

Figure 1 shows the ratio of T_m/T for high transmission conditions. Lower transmissions are not shown because multiple scattering effects become important and the model is not appropriate. As seen in Figure 1, particles less than $50 \mu\text{m}$ minimally impact the transmittance ratio and, therefore, their diffraction peak contributions are not important within the FOVs of the ABL system. The (minor) differences between the high energy COIL and the tracking lidar are from the different FOVs. Larger particles ($250 \mu\text{m}$), on the other hand, can scatter appreciable energy within the FOV of the imaging/tracking (ATP) sensor system. However, the optical depths associated with these particles will render the system inoperable in any case.

Table 4. Size Parameters and Forward Scattering Correction Factors for Different Aerosol Types

AEROSOL TYPE	TYPICAL LENGTH (μm)	SIZE PARAMETER	CORRECTION FACTOR- D'	
			HEL	Tracking
B'ground Stratospheric	0.5	1.21	0.000	0.016
Thin cirrus	50.0	121	0.006	0.050
Cirrus	250.0	604	0.081	0.210

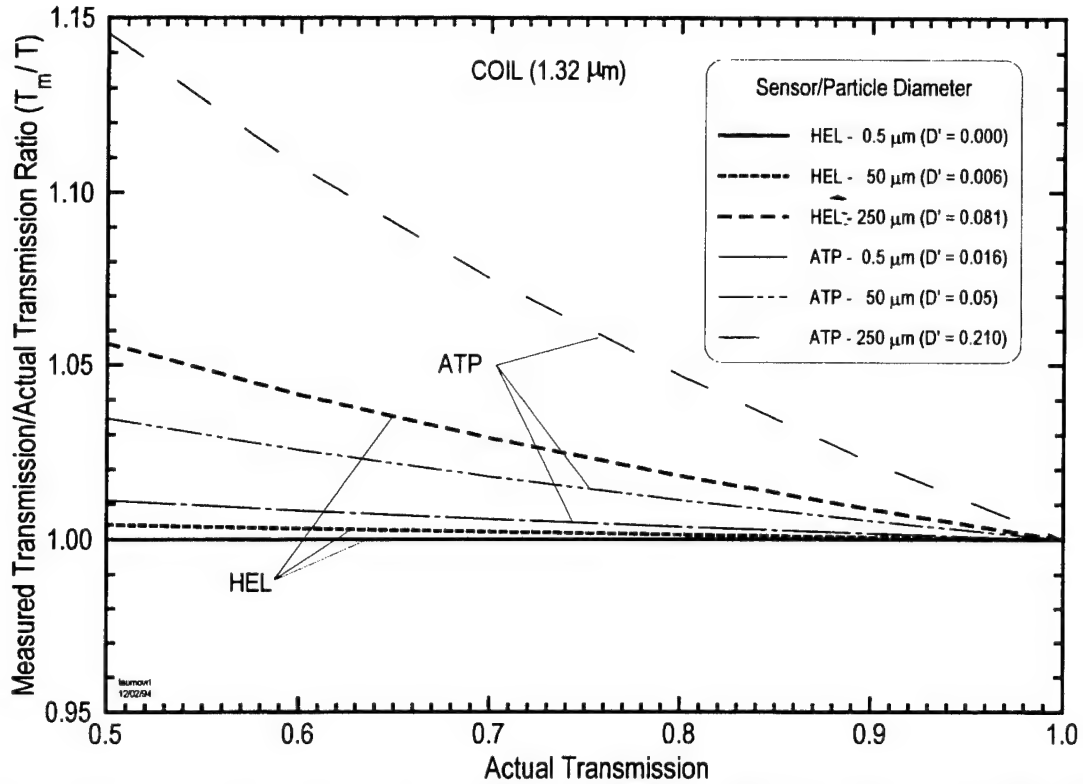


Figure 1. Apparent to Actual Transmittance Ratio for Different Particle Sizes and ABL Field-of-View Conditions. The apparent transmittance includes single scattering contributions from the particle diffraction peak. Ratios for $T < 0.50$ are not shown because multiple scattering effects become important.

2.3 Multiple Forward Scattering Effects

This section assesses aerosol multiple forward scattering effects on the ABL system. In particular, the governing equations are subject to the multiple small-angle scattering approximation which assumes that there are no scattered energy losses in the lateral or backward directions.

2.3.1 Aerosol Modulation Transfer Function

The aerosol modulation transfer function (M_{aer}) is the basis for evaluating aerosol forward scattering effects in a scattering medium of known optical depth. Physically, M_{aer} describes the cross-correlation of optical fields (due to aerosol scattering) that are separated by a distance ρ in the transverse direction.⁸ M_{aer} is analogous to the well-known modulation transfer function for turbulence.

The current study assumes that a uniform aerosol medium exists between the transmitter and the target plane. For these conditions, M_{aer} is expressed as⁸

$$M_{aer}(\rho, \tau_{scl}) = \exp(-\tau_{scl}) + [1 - \exp(-\tau_{scl})]M_{scl}(\rho, \tau_{scl}) . \quad (4)$$

An interpretation of Eq. 4 is shown in Figure 2. Effectively, the first term attenuates the beam intensity and the second term accounts for contributions from multiple small-angle scattering. In the second term, M_{scl} equals

$$M_{scl}(\rho, \tau_{scl}) = \frac{\exp\{-\tau_{scl}[1 - f(\rho)]\} - \exp(-\tau_{scl})}{1 - \exp(-\tau_{scl})} \quad (5)$$

where for spherical wave propagation, $f(\rho)$, is given by

$$f(\rho) = \frac{1}{4\pi} \int_{4\pi} P(\theta) d\Omega \int_0^1 J_0(k\rho u \sin \theta) du . \quad (6)$$

In Eq. 6, k is the laser wavenumber ($2\pi/\lambda$, with λ equal to the wavelength of radiation), $d\Omega$ is the incremental solid angle, and J_0 is the Bessel function of the first kind and order zero. For scattering predominantly in the forward direction, it can be shown that

$$M_{scl}(\rho, \tau_{scl}) \approx \exp - (\rho / \rho_a)^2 \quad (7)$$

where ρ_a is the $(1/e)$ transverse coherence length through an aerosol scattering medium of optical thickness τ_{scl} . The transverse coherence length, ρ_a , is calculated using the expression in Eq. 7 once M_{scl} is obtained from Eq. 5.

Using aerosol phase functions from LOWTRAN7 and a scattering optical depth equal to 1, Eq. 5 was numerically solved for background stratospheric aerosols and cirrus. Figure 3 shows M_{scl} for these two aerosols at visible wavelengths. The cirrus has a larger transverse coherence length (ρ_a), due to its larger particle sizes. In each case however, ρ_a is on the order of one micron.

Values of ρ_a were then obtained for other scattering optical depths. Figure 4 shows the transverse coherence length at visible wavelengths as a function of the scattering optical depth for background stratospheric aerosols and cirrus. Figure 5 shows the same plot at ABL wavelengths. All coherence lengths are less than 6 μm for optical depths between 0.1 and 10. For comparison purposes, turbulence coherence lengths are on the order of a few tens of centimeters for ABL scenarios.

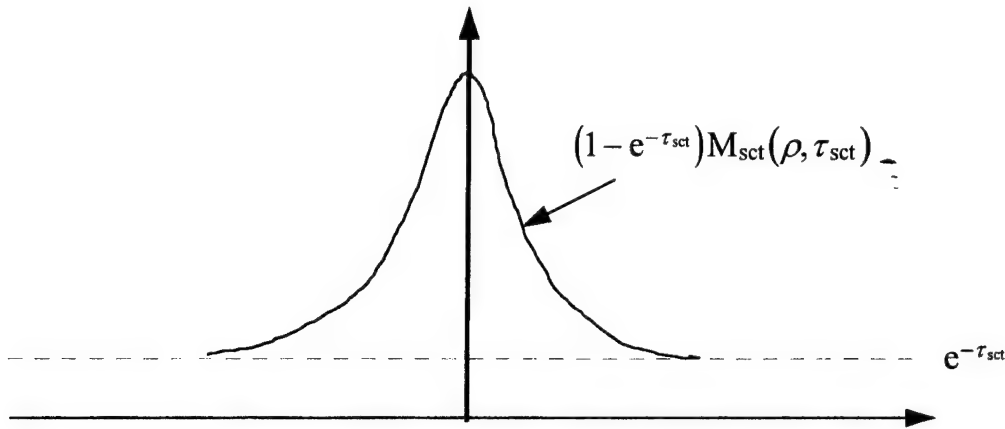


Figure 2. Conceptual Form of the Aerosol Modulation Transfer Function, M_{aer} . The figure is adapted from Reference 8.

2.3.2 Angular Extent of Aerosol Multiple Forward Scattering

A knowledge of the transverse coherence length (ρ_a) was used to estimate the angular extent of aerosol multiple forward scattering. Specifically, the scattering divergence half-angle, which represents the angular extent of the halo surrounding a point image, is

$$\theta_{sct} = \frac{\lambda}{\pi \rho_a} \quad (8)$$

where λ is the wavelength of radiation. Using values of ρ_a (see Figures 4 and 5), the scattering divergence half-angles as a function of scattering optical depth are shown in Figures 6 and 7 for visible and ABL wavelengths, respectively. Scattering half-angles are relatively large, ranging from 0.07 rad to 1 rad. When compared with the divergence angle of a typical laser beam (on the order of microradians), aerosol multiple forward scattering effects occur well outside the diffraction beam spread due to the transmitter. Thus, aerosol multiple forward scattering effects cannot contribute significantly to the energy delivered by the (highly focused) COIL laser. In regards to image blurring and adaptive optics, the impact on the ABL tracking lidar will be minimal because most of the scattering energy is spread over scattering angles well outside the field-of-view (which is on the order of milliradians).

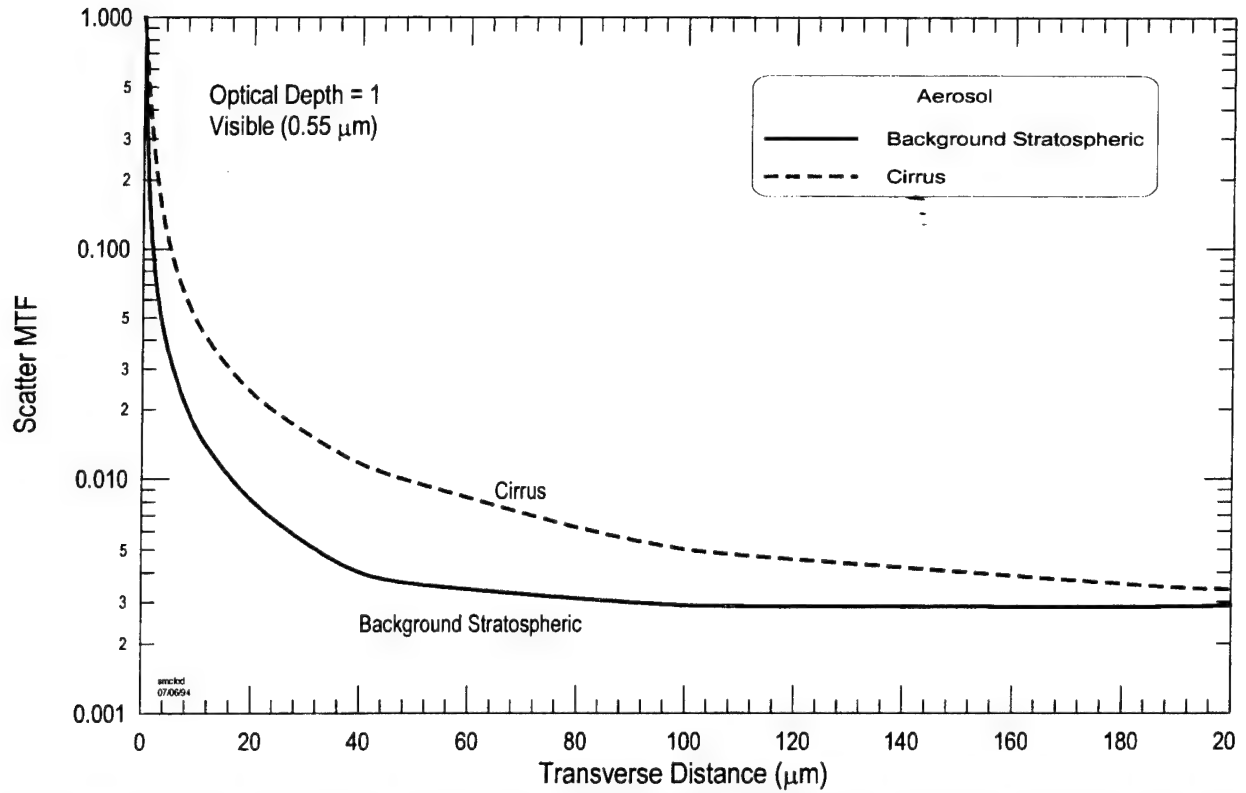


Figure 3. Multiple Scattering Component of the Aerosol Modulation Transfer Function (M_{sct}) for Background Stratospheric Aerosols and Cirrus

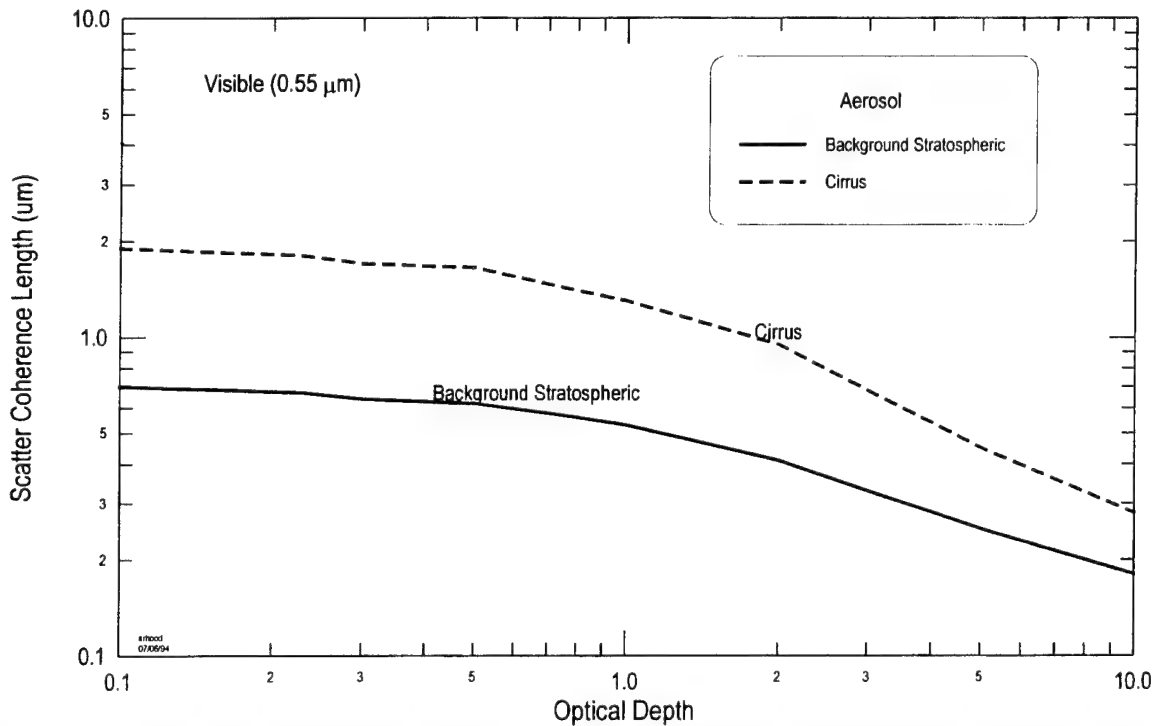


Figure 4. Transverse Coherence Length (ρ_a) as a Function of Scattering Optical Depth at Visible Wavelengths

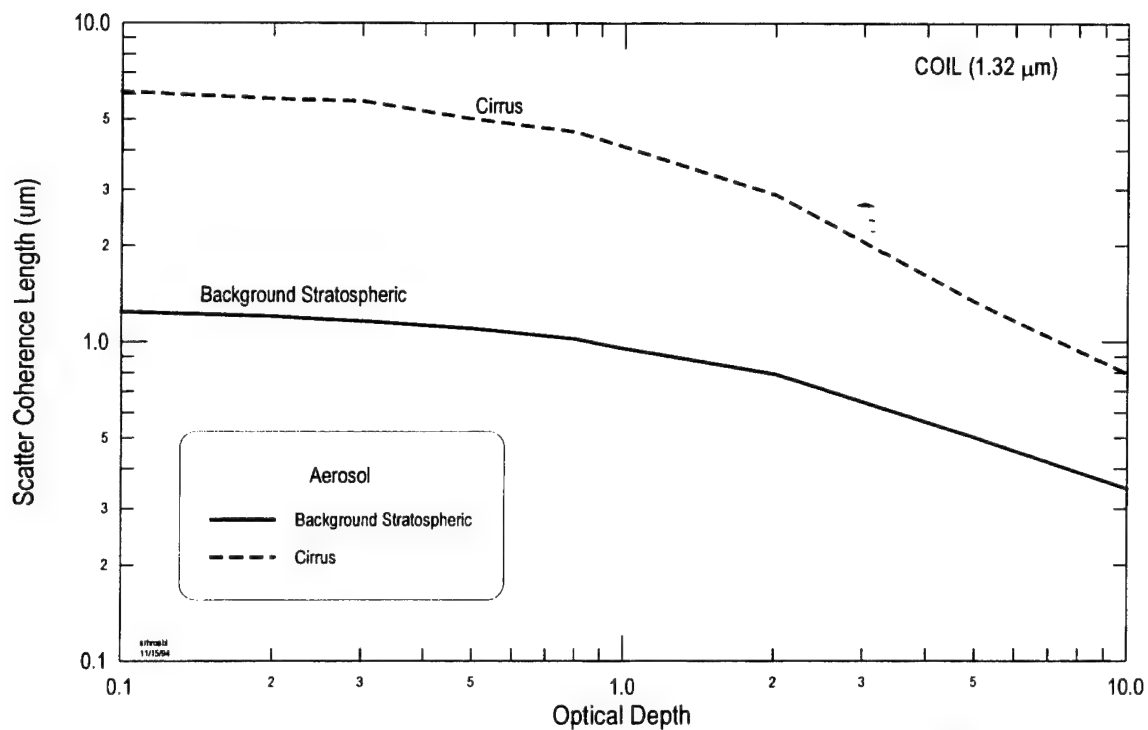


Figure 5. Transverse Coherence Length (ρ_a) as a Function of Scattering Optical Depth at ABL Wavelengths

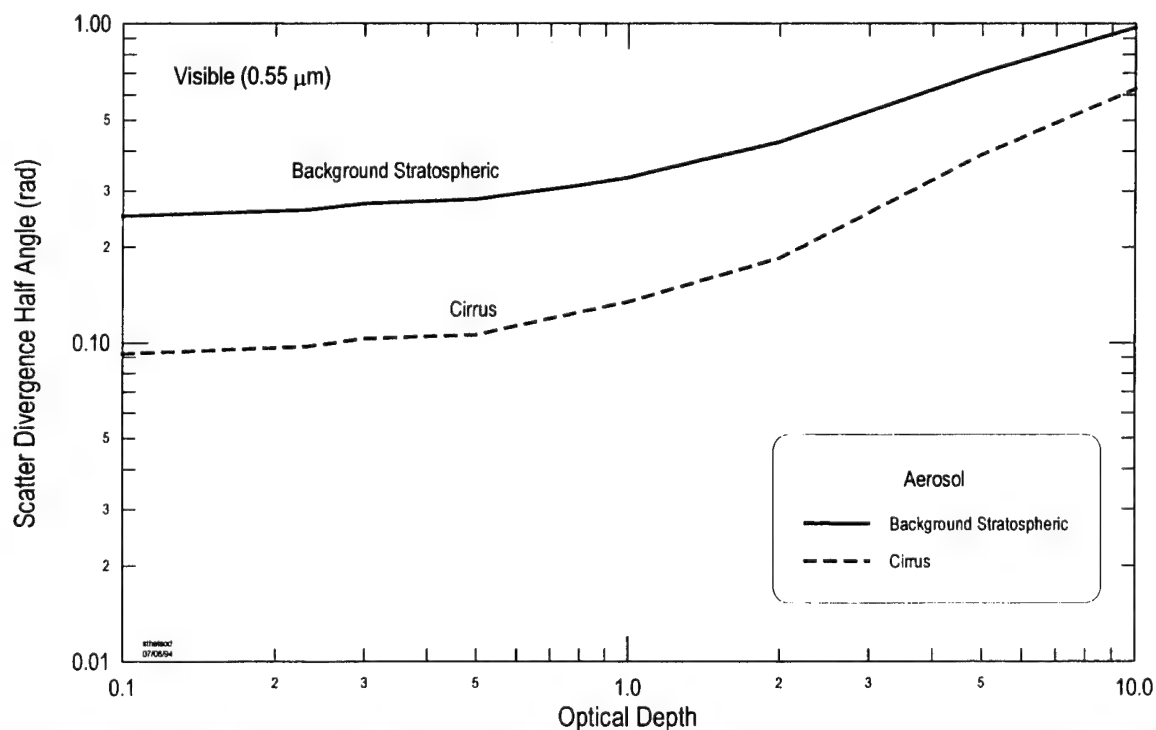


Figure 6. Scattering Divergence Half-Angle as a Function of Scattering Optical Depth at Visible Wavelengths

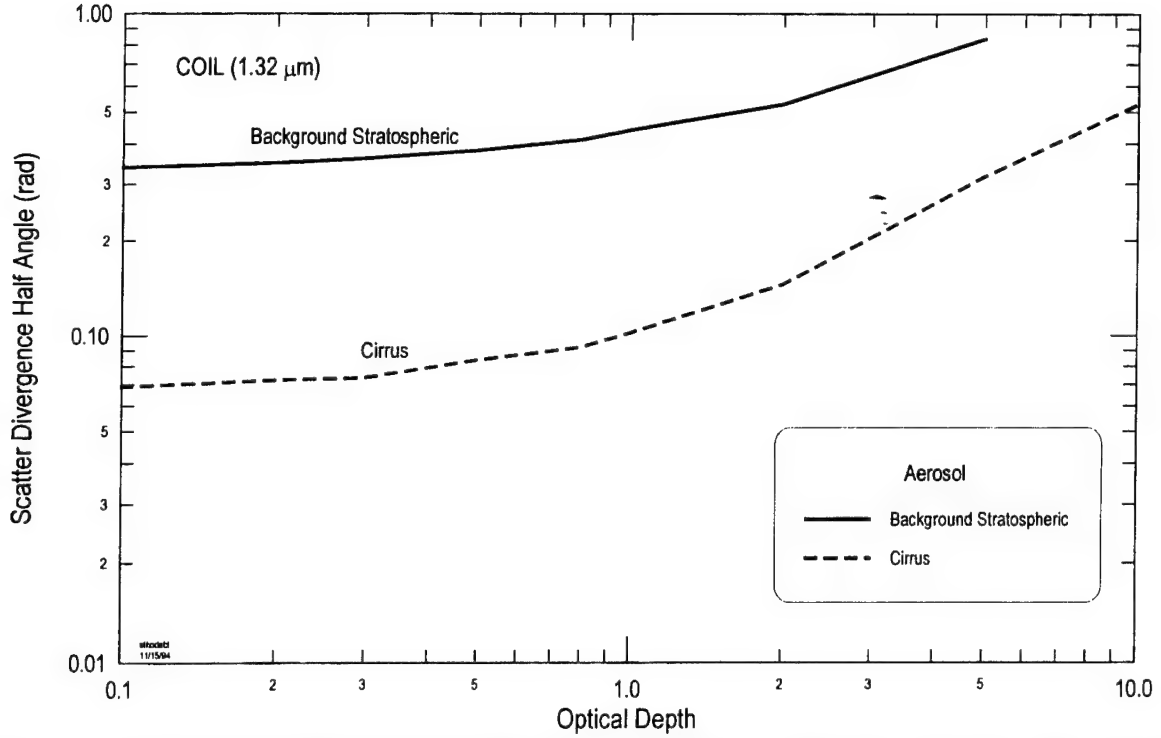


Figure 7. Scattering Divergence Half-Angle as a Function of Scattering Optical Depth at ABL Wavelengths

2.3.3 Aperture Effects

The impact of aperture size on aerosol multiple forward scattering effects was investigated. The diffraction-limited divergence half-angle, θ_d , for a transmitter (Gaussian beam) or receiver is given as

$$\theta_d = \frac{2\lambda}{\pi D} \quad (9)$$

where D is the aperture diameter. At a distance z from the transmitter or receiver, the diffraction-limited $1/e$ spot size (r_d) is

$$r_d = \theta_d z \quad (10)$$

and the diffraction-limited irradiance at distance z and transverse radius r is proportional to

$$I_d(r, z) \propto \frac{\exp(-\tau_{sc})}{\theta_d^2} \exp(-r^2 / r_d^2) \quad (11)$$

for any type of beam which has a far field Gaussian shape including a uniformly illuminated beam or a point source. Similarly, the irradiance due to multiple scattering is proportional to

$$I_{sct}(r, z) \propto \frac{1 - \exp(-\tau_{sct})}{\theta_{sct}^2} \exp(-r^2 / r_{sct}^2) \quad (12)$$

where $r_{sct}(=\theta_{sct} z)$ is the $1/e$ spot radius due to multiple scattering. Therefore, the ratio (\mathfrak{R}) of the peak diffraction-limited spot intensity to the peak scatter intensity is

$$\mathfrak{R} = \frac{I_d}{I_{sct}} = \frac{\exp(-\tau_{sct})}{1 - \exp(-\tau_{sct})} \left(\frac{\theta_{sct}}{\theta_d} \right)^2. \quad (13)$$

Figures 8 and 9 show values of \mathfrak{R} at visible and ABL wavelengths, respectively, as a function of scattering optical depth for a 10 cm receiver imaging a point source. Extremely large ratios for small optical depths (τ_{sct}) exist because of the large differences between the diffraction and scattering divergences. At large optical depths, the ratio decreases primarily due to transmission losses through the medium. As seen in Figure 10, the ratios at visible wavelengths lower by a factor of 100 if a 1 cm receiver is used instead. For a 50 cm ABL diameter, values of \mathfrak{R} at ABL wavelengths increase by a factor of 25 over that of a 10 cm ABL diameter as expected since it is just due to the ratio of the diameters squared (see Figure 11). These results imply that it takes extremely large optical depths to have multiple scattering irradiances comparable to diffraction/focusing effects, although it is the reduced transmission of the unscattered beam that reduces the ratio.

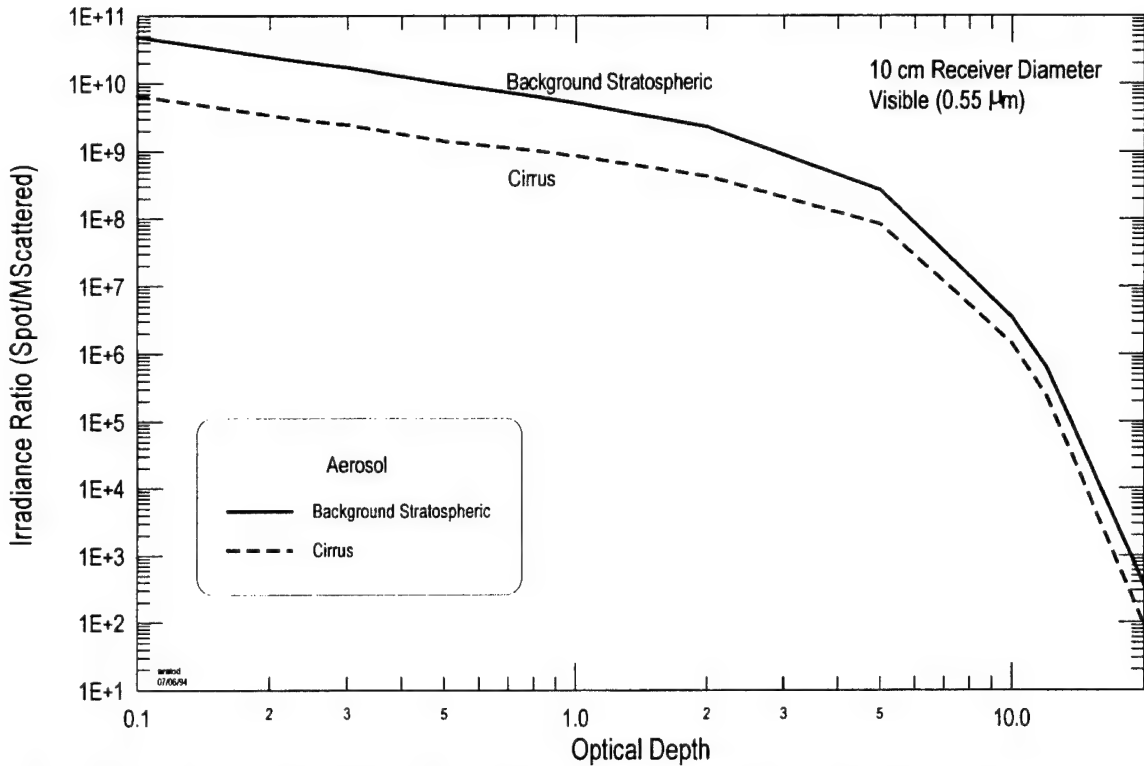


Figure 8. Ratio of the Visible Peak Diffraction-Limited Spot Intensity to Peak Multiple Scatter Intensity as a Function of Scattering Optical Depth for a 10 cm Diameter Receiver

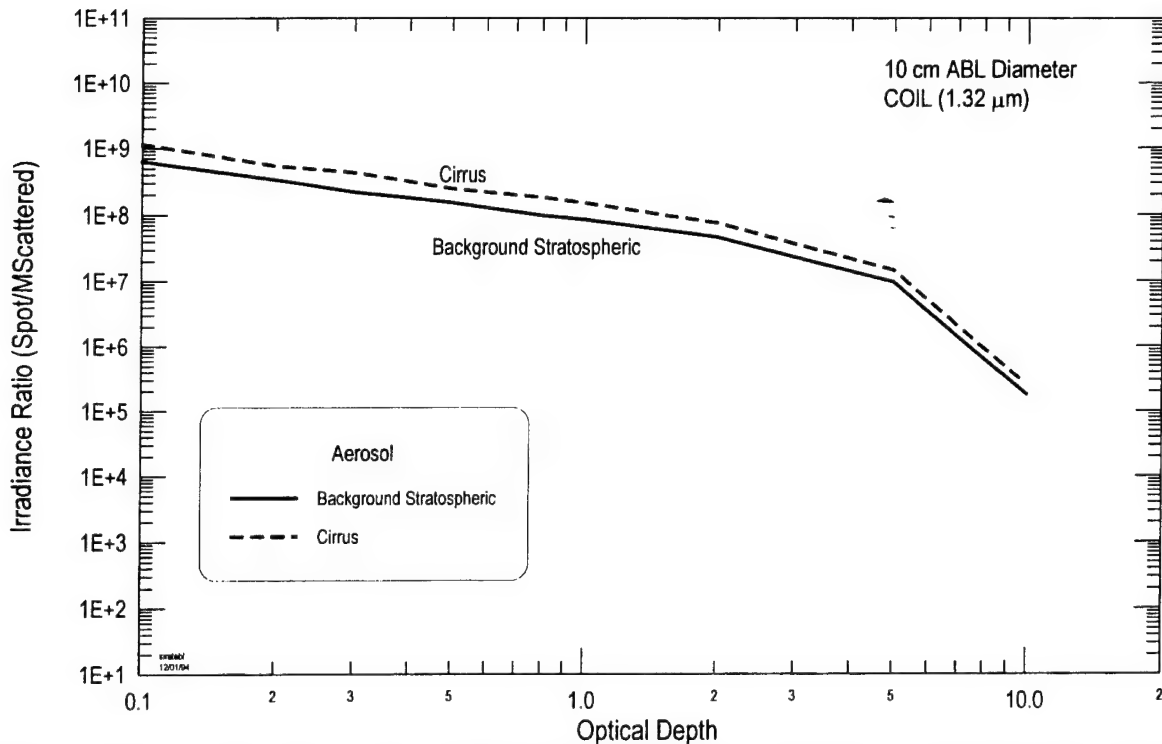


Figure 9. Ratio of the ABL Peak Diffraction-Limited Spot Intensity to Peak Multiple Scatter Intensity as a Function of Scattering Optical Depth for a 10 cm ABL Diameter

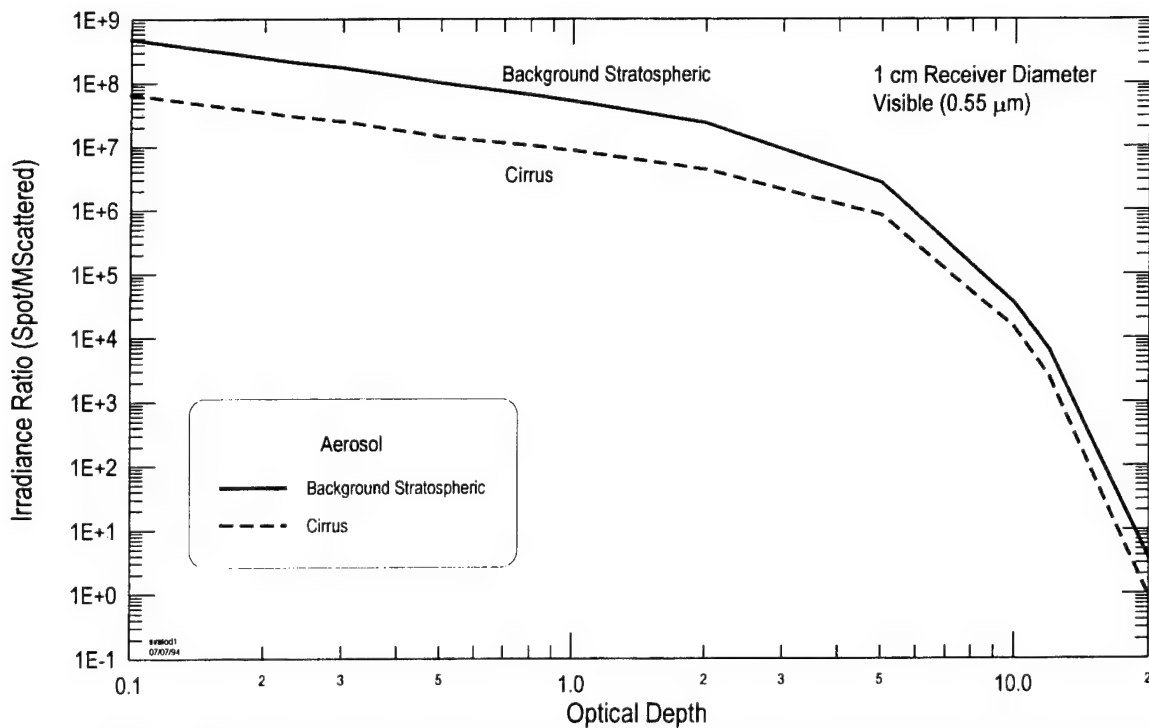


Figure 10. Ratio of the Visible Peak Diffraction-Limited Spot Intensity to Peak Multiple Scatter Intensity as a Function of Scattering Optical Depth for a 1 cm Diameter Receiver. Note ordinate scale is different from other figures comparing irradiance ratios

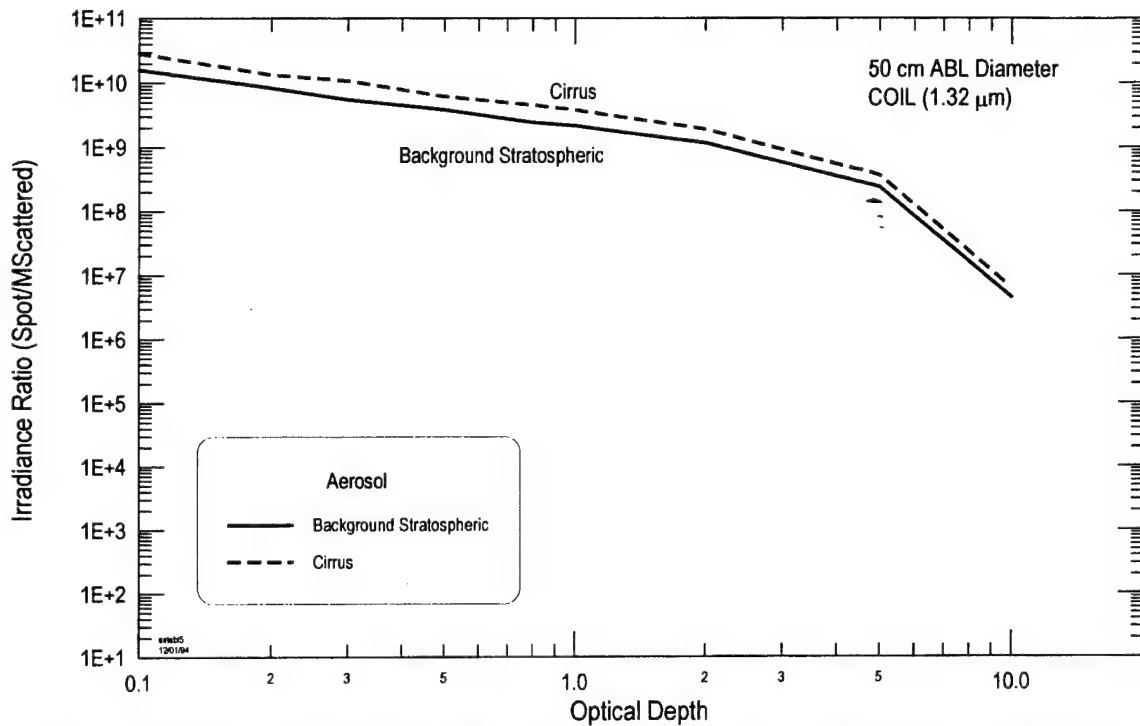


Figure 11. Ratio of the ABL Peak Diffraction-Limited Spot Intensity to Peak Multiple Scatter Intensity as a Function of Scattering Optical Depth for a 50 cm ABL Diameter

Using the multiple small-angle scattering assumptions, the optical depth at which the incoherent radiant intensity equals the peak intensity of the remaining coherent radiation can be estimated.¹⁴ For monodisperse aerosols, the relationship at visible wavelengths is

$$\tau \omega_o \approx 2 \ln \left(\frac{0.963 D}{2a} \right) + \ln \left[2 \ln \left(\frac{0.963 D}{2a} \right) \right] \quad (14)$$

where a is the particle radius, τ is the total aerosol optical depth (scattering plus absorption), and ω_o is the aerosol single scattering albedo. Figure 12 shows an application of Eq. 14 for ω_o equal to 1 (no absorption). The required scattering optical depths are greater than 10 for apertures greater than 1 cm and particles on the order of 10 of microns, or less.

¹⁴ Accetta, J.S., and Shumaker, D.L. (Chief Eds.) (1993) *The Infrared and Electro-Optical Systems Handbook, Volume 7, Countermeasure Systems*, D. Pollock (Ed.), Chapter 6, *Obscuration Countermeasures* by D.W. Hooch, Jr. and R.A. Sutherland, ERIM Infrared Information Analysis Center and SPIE Optical Engineering Press (Copubl.), Ann Arbor, Michigan and Bellingham, Washington, pp. 412-417.

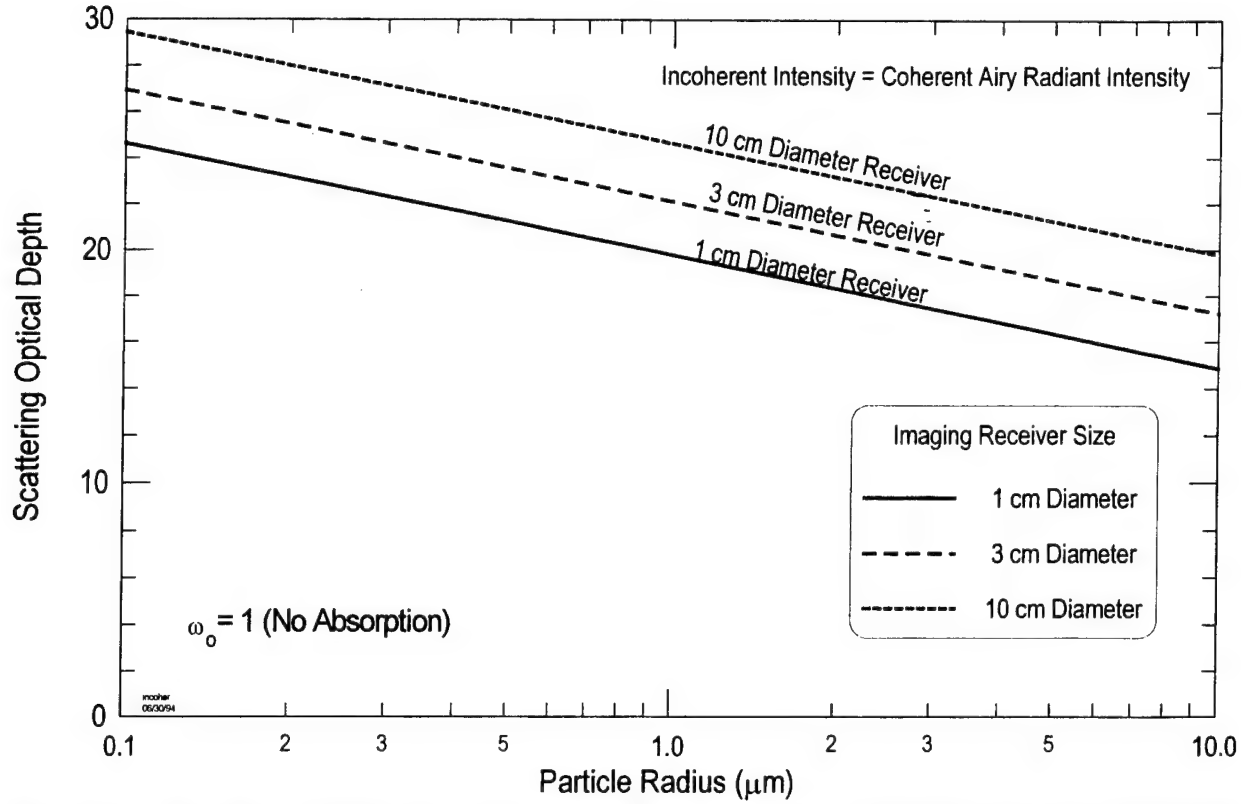


Figure 12. Scattering Optical Depth Required for Equal Peak Intensities Due to Incoherent Scattering and Diffraction Effects for a Monodisperse Aerosol

2.3.4 Beam Spread Pattern from Aerosol Multiple Forward Scattering

The aerosol modulation transfer function was used to estimate the beam spread pattern (due to aerosol multiple forward scattering) for a collimated laser beam. Specifically, the average irradiance $\langle I \rangle$ at a distance r from the optic axis of a transmitter in a target plane located at range z equals⁸

$$\langle I(r, z) \rangle = \left(\frac{k}{2\pi z} \right)^2 P \int M_{trans}(\rho) M_{aer}(\rho, \tau_{sct}) \exp\left(-\frac{ik}{z} r \cdot \rho\right) d^2 \rho \quad (15)$$

where P is the total radiated power, k is the laser wavenumber ($2\pi/\lambda$), and M_{trans} is the modulation transfer function for the transmitting aperture. Because Eq. 15 assumes a collimated laser beam, it only estimates the high energy COIL because the latter invokes focusing and possibly adaptive optics. For the purposes of evaluating Eq. 15, the transmitter emits a collimated beam with a Gaussian aperture field. The corresponding expression for M_{trans} equals

$$M_{trans}(\rho) = \exp(-\rho^2 / 4W_o^2) \quad (16)$$

where W_o is the $1/e$ aperture intensity radius. For vacuum propagation ($M_{aer}(\rho, \tau_{scf})=1$), Eq. 15 has an analytic solution of

$$\langle I(r, z) \rangle = \frac{P}{\pi W_{vac}^2} \exp(-r^2 / W_{vac}^2) \quad (17)$$

where W_{vac}^2 equals

$$W_{vac}^2 = W_o^2 [1 + (z / kW_o^2)^2] \quad (18)$$

Beam spread patterns were calculated as a function of scattering optical depth using Eq. 15. Aerosol phase functions were approximated with the Henyey-Greenstein formulation¹⁵

$$P_{HG}(\cos \theta) = \frac{1 - g^2}{4\pi(1 + g^2 - 2g \cos \theta)^{3/2}} \quad (19)$$

where g is the aerosol asymmetry parameter. The Henyey-Greenstein formulation is used in LOWTRAN7 to estimate the phase function for thin cirrus. The analysis was performed for a W_o of 1 mm and wavelength of 0.55 μm . The small value of W_o was necessary due to computer memory limits with the Fourier Transform (see Appendix A). In the context of Eq. 16 however, a more suitable W_o for the high energy COIL (~ 10 cm) only reduces the angular width of the calculated transmitter diffraction peak. Using Eq. 17 evaluated $z=0$, the effective aperture diameter D is about 3.0 mm. The analysis expresses Eq. 15 in terms of the relative irradiance as a function of off-axis angle, so the range dependence normalizes out.

Figure 13 shows the beam spread pattern for scattering optical depths between 0 and 5. The aerosol asymmetry parameter is set to 0.95 which represents an upper limit of forward scattering by thin cirrus. For vacuum propagation ($\tau_{scf}=0$), the calculated intensity becomes small at an off-axis angle of about 0.15 mrad which agrees with the diffraction-limited divergence angle ($=2\lambda/\pi D$). Figure 13 indicates that aerosol multiple scattering spreads the beam energy beyond the diffraction-limited divergence angle. As the scattering optical depth increases, the diffraction peak is attenuated and more beam energy is scattered towards off-axis angles beyond about 10 mrad. Of particular interest to the high energy COIL, Figure 13 also excises aerosol multiple forward scattering effects near the optical axis of the transmitter. That is, any departures from the transmitted intensity, $\exp[-\tau_{scf}]$, are due to aerosol multiple forward scattering. As seen in Table 5, aerosol multiple forward scattering contributes very little to the on-axis intensity for $\tau_{scf} < 5$ and $g=0.95$. Effectively, the RMS scattering angles, $\sim 30^\circ$, are too large for multiple scattered energy to remain along or near the optical axis. The (small) multiple scattering component decreases as τ_{scf} increases because each scattering event directs previously scattered energy away from the optical axis.

Figure 14 shows how the shape of the aerosol phase function impacts the beam spread pattern. (The scattering by an aerosol with $g=0.70$ is less peaked in the forward direction than an

¹⁵ Henyey, L., and Greenstein, J. (1941) Diffuse radiation in the galaxy, *Astrophys. J.*, **93**: 70-83.

aerosol with $g=0.95$.) Aerosol multiple forward scattering effects within the transmitter diffraction peak are smaller when the aerosol (inherently) scatters more energy towards wider angles, although the differences between $g=0.70$ and 0.95 are almost negligible. Also, for a fixed τ_{sct} , more beam energy is scattered further from the optical axis (>100 mrad) when the scattering is less peaked in the forward direction.

2.4 Impact of Inhomogeneous Scattering on the Beam Spread Pattern

In general, the aerosol medium for an ABL engagement will be inhomogeneous and the system performance may depend on the relative position (along the path) of a pronounced scattering feature, such as cirrus. When a point source is viewed through a thin diffuse scattering layer, for example, the image becomes more fuzzy when the layer is further from the point source (*i.e.*, the “shower curtain” effect).¹⁶

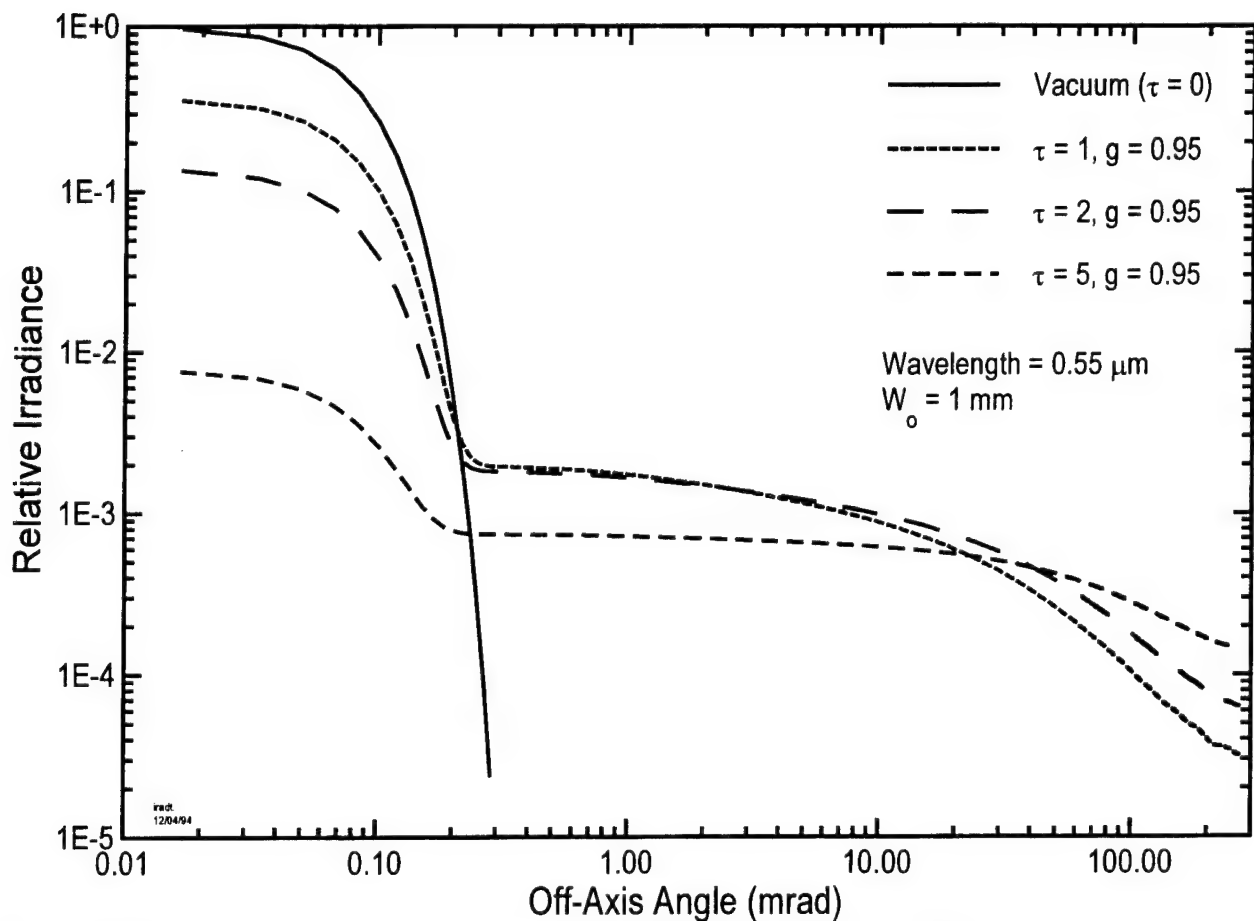


Figure 13. Beam Spread Pattern as a Function of Scattering Optical Depth

¹⁶ Bohren, C.F. (1991) *What Light Through Yonder Window Breaks?*, John Wiley & Sons, New York, New York, p. 148.

Table 5. Comparison of the On-Axis Transmitted Intensity Against the Calculated On-Axis Intensity as a Function of Scattering Optical Depth. The differences are due to aerosol multiple forward scattering effects

SCATTERING OPTICAL DEPTH	TRANSMITTED INTENSITY	ON-AXIS INTENSITY	DIFFERENCE
1	0.3678	0.3735	0.0057
2	0.1353	0.1398	0.0045
5	0.0067	0.0078	0.0011
5	0.0067	0.0073 [†]	0.0006

[†] $g = 0.70$

Due to the level of effort in this study, Eq. 15 could not be extended to inhomogeneous media. However, a "back-of-the-envelope" analysis looked at the spread of a "narrow" beam after it encounters a thin diffuse layer (see Figure 15). In the figure, D_1 is the transmitter-to-layer distance, D_2 is the layer-to-missile distance, and the RMS scattering angle, θ_{rms} , describes the angular extent of aerosol scattering by the diffuse layer (see Section 2.2.1). In the missile

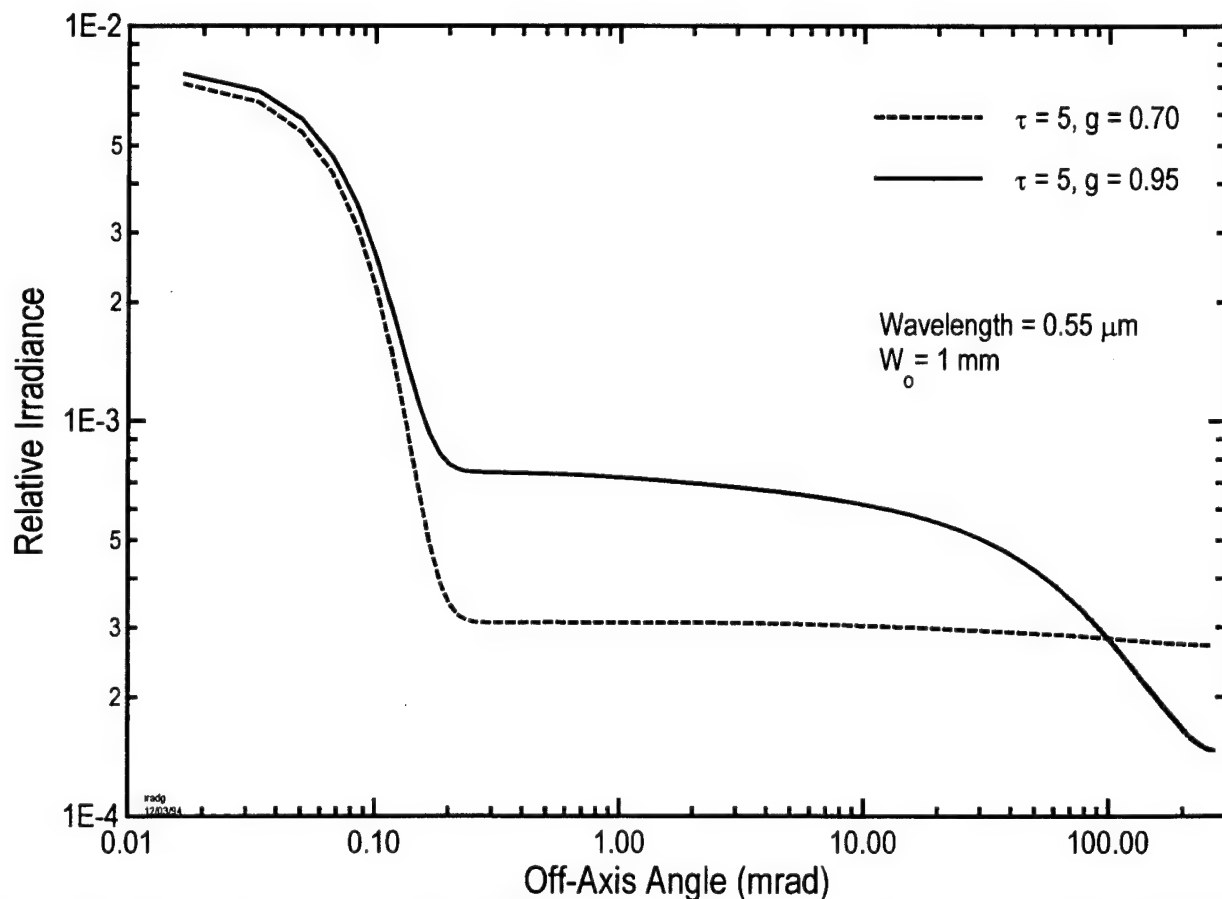


Figure 14. Beam Spread Pattern For Different Aerosol Asymmetry Parameters. A g of 0.70 is representative of a background stratospheric aerosol

plane, the radius of the beam is

$$R = D_2 \tan \theta_{rms} \quad (20)$$

and the half-angle beam spread due to scattering is

$$\theta_s = \tan^{-1} \frac{R}{D_1 + D_2} = \tan^{-1} \frac{D_2 \tan \theta_{rms}}{D_1 + D_2} \quad (21)$$

as measured from the transmitter. Although the scattering geometry in Figure 15 only considers single scattering, it can be used qualitatively to assess aerosol forward scattering effects.

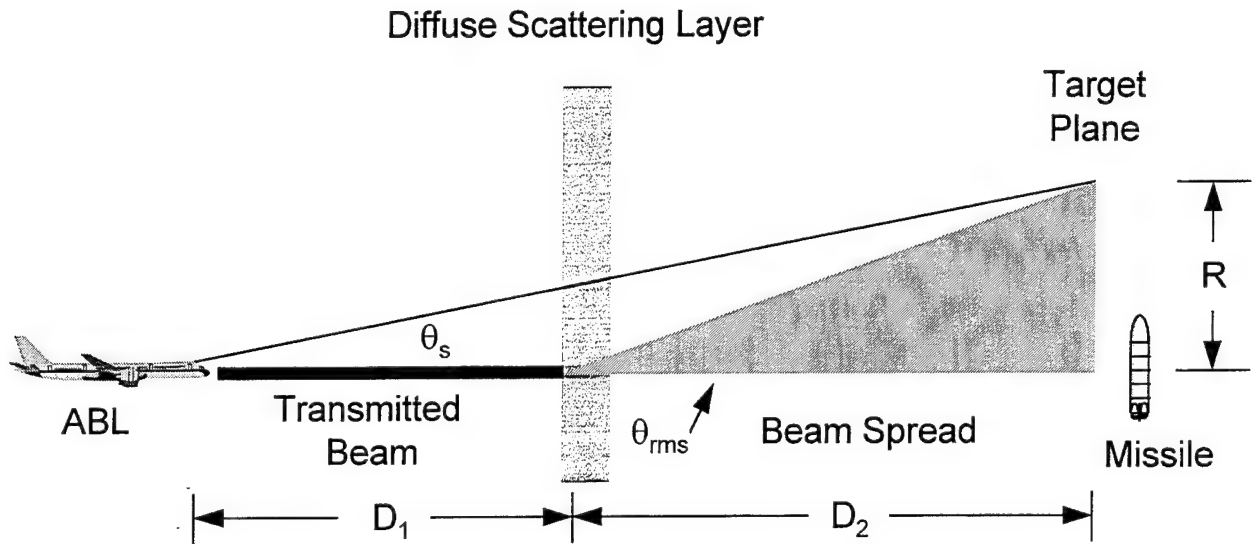


Figure 15. Scattering Geometry of a "Narrow" Beam As It Encounters a Thin Diffuse Scattering Layer. There is no beam focusing or divergence. The figure is not drawn to scale.

Figure 16 shows the angular beam spread, θ_s , as a function of transmitter-to-layer distance. The two notional transmitter-to-missile distances considered are 100 and 500 km and the RMS scattering angles characterize thin cirrus (30.2°) and background stratospheric aerosols (51.6°), see Table 3. The trends in Figure 16 indicate that the angular dimensions of the spread due to scattering far exceed typical beam divergences for HEL systems (on the order of microradians), except when the layer is very close to the missile. Thus, aerosol forward scattering effects do not impact the energy delivered to the missile because scattered energy is lost well outside the transmitted energy field. Furthermore, the situation in which θ_s becomes small is extremely unlikely because cirrus are more likely to be closer to the aircraft (*i.e.*, transmitter) than the missile.

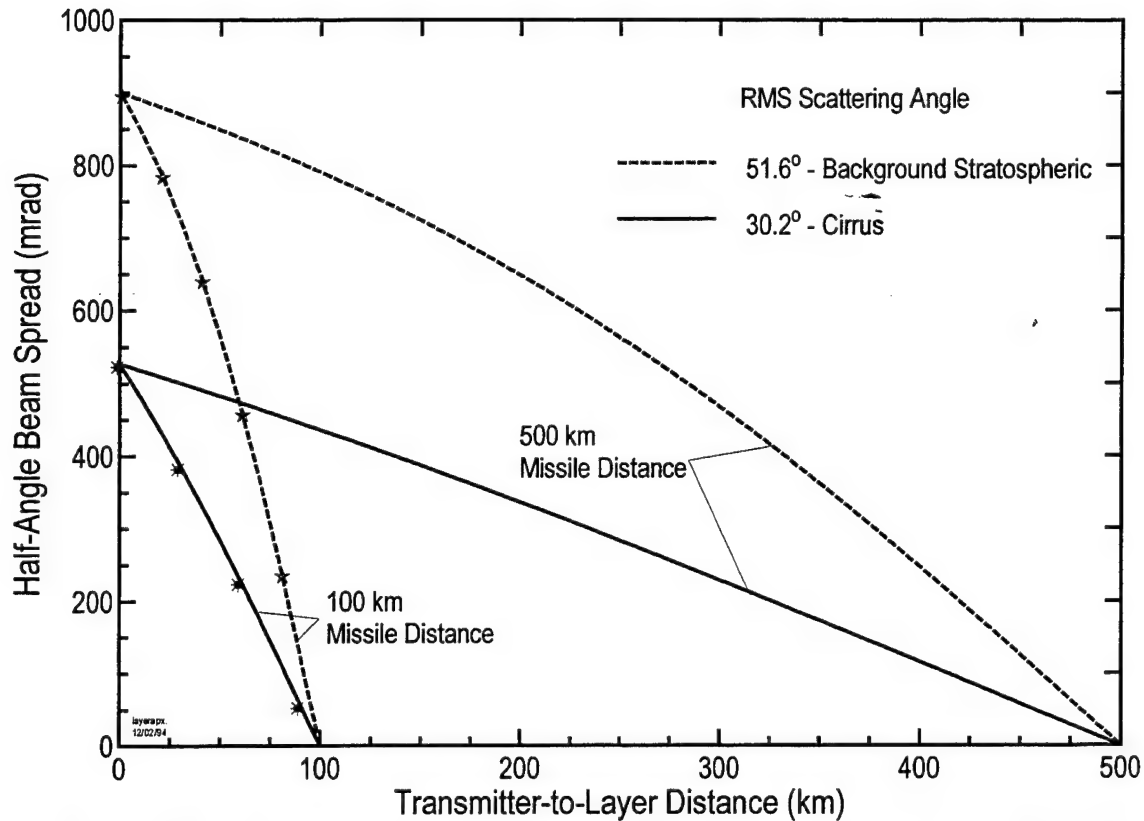


Figure 16. Half-Angle Beam Spread Due to a Thin Scattering Layer as a Function of Transmitter-to-Layer Distance. The transmitter-to-missile distances are 100 and 500 km. For comparison, beam spreads for typical HEL systems are microradians

3 LITERATURE SURVEY

A number of experiments in the open scientific literature address the angular extent of aerosol forward scattering. Although visible wavelengths are frequently used, the scattering behavior can be extended to ABL wavelengths, at least in general terms. Also, the driving force for most of these experiments is image blurring by forward-scattered radiation, rather than the potential impact on laser weapon propagation. However, the loss of image sharpness and/or contrast (for a point source against a dark background) indicates some degree of aerosol forward scattering near the optical axis. The blurring can result from single or multiple scattered radiation, although it requires highly-peaked phase functions in the forward direction. Given such a scattering medium, aerosol forward scattering could adversely impact a (narrow beam) HEL system in regards to coherence loss and/or beam broadening near the optical axis.

3.1 Experiment Summary

Bissonnette¹⁷ conducted a simple experiment in which the images of unresolved point sources were observed in nighttime haze, radiation fog, advection fog, and rain conditions. In particular, an imaging system recorded digitized images of sources at horizontal distances of 531 and 921 m across flat grassy terrain. These distances are much shorter than those for the ABL engagements, but effectively it is the optical depth and particle size that determine the angular spread of aerosol forward scattering.

Table 6 summarizes the observed aerosol forward scattering effects for different aerosol events. Clear air measurements estimated the e^{-2} width of the source central peak to be ~ 0.14 mrad at both distances. For most weather events, the measuring capability of the system extended to 1.2 mrad off-axis.

Table 6. Aerosol Forward Scattering Effects on a Point Source During Different Aerosol Events as Reported by Bissonnette.¹⁷ The mode radii come from curve fits of measured particle distributions. The 5% peak width is the calculated scattering angle where the aerosol phase function reaches 5% of its peak value. The measured optical depths come from a wide spectral range transmissometer

OBSERVED AEROSOL EVENT	APPROX. MODE RADII	APPROX. 5% PEAK WIDTH (deg)	MEASURED OPTICAL DEPTH	OBSERVED EFFECT OF FORWARD SCATTERING (Relative to Peak Intensity)
Haze	0.35 μm	70	0.19 at 531 m 0.33 at 921 m	None None
Radiation fog (plus many advection fogs)	0.35 and 13 μm	7.1	1.98 at 531 m 3.67 at 921 m 3.97 at 531 m 7.22 at 921 m	None None Very little Very little
One event with advection fog/light rain	1.0 and 45 μm , with many 100 μm particles	0.45	4.47 at 531 m 8.60 at 921 m	1% at and beyond source e^{-2} width 10% at and beyond source e^{-2} width
Rain	1000.0 μm	0.04	0.91 at 531 m 1.96 at 921 m	10% at source e^{-2} width, less beyond 10% at source e^{-2} width, less beyond

Recent work by Linskens and Bohren¹⁸ has asserted that a unique combination of large particles (compared with the wavelength of radiation) and moderate optical depth is sufficient to explain why the solar disk sometimes appears fuzzy when viewed through thin clouds. The fuzzy sun phenomenon pertains to the ABL case because it indicates aerosol forward scattering

¹⁷ Bissonnette, L.R. (1992) Imaging through fog and rain, *Optical Engineering*, **31**:1045-1052.

¹⁸ Linskens, J.R., and Bohren, C.F. (1994) Appearance of the sun and moon seen through clouds, *Applied Optics*, **21**: 4733-4740.

effects are competing with the transmitted intensity field at angles near the line-of-sight (the solar half-angle width is about 0.25 deg or 4 mrad).

Linskens and Bohren conducted controlled experiments in which a light bulb was viewed through a glass tank filled with distilled water and a suspension of particles similar (in size) to typical atmospheric aerosols. The viewing distance to the light bulb simulated the solar angular width. As particles were added to the tank, the image of the light bulb was noted. Table 7 describes the appearance of the light bulb for particle suspensions of different size and optical depths. Note that the Linskens and Bohren experiment gives "more or less" results because it is based on visual perception.

Table 7. Appearance of a Light Bulb As Viewed Through a Scattering Medium from Linskens and Bohren.¹⁸ The corona and aureole are pronounced (single scattering) diffraction features

SIMULATED AEROSOL	MEAN RADIUS	OPTICAL DEPTH	OBSERVATIONS OF LIGHT BULB IMAGE
Haze	$0.326 \pm 0.0024 \mu\text{m}$	<8.4	Sharp edge on image, no aureole or corona
		8.8	Image edge appears fuzzy
		9.4	Image indistinguishable from background
Fog	$2.65 \pm 0.6 \mu\text{m}$	1.2	Sharp edge on image; 1.5° aureole and corona become visible
		7.5	Sharp edge on image; corona not visible
		10.9	Image edge appears fuzzy
		11.8	Image indistinguishable from background
Clouds	$7.9 \pm 1.45 \mu\text{m}$	Few drops	Sharp edge on image; aureole and corona (<1.5°) become visible
		5.2	Sharp edge on image; corona not visible
		9.8	Image edge appears fuzzy
		12.8	Image indistinguishable from background

3.2 Comparisons Against Current Results

The experiments summarized above encompass particle sizes and optical depths to be encountered at ABL altitudes. For completeness, the current assertions about aerosol forward scattering must be validated against and consistent with the observations from these experiments.

Tables 6 and 7 support the assertions developed in the current study. Table 6 suggests that for small aerosols (similar in size to background aerosols, volcanic aerosols, and thin cirrus), the measured intensity equaled the transmitted intensity within milliradians of the optical axis. Aerosol forward scattering effects only occurred when ample numbers of particle greater than $50 \mu\text{m}$ existed in the scattering medium--a situation that does not readily occur at ABL altitudes except in thick cirrus. Given the ~70% transmission criterion for ABL operation, however, the ABL system will not operate in thick cirrus because the associated transmissions are too low. Table 7 indicates that for small aerosols, multiple forward scattering effects (apparent as image fuzziness) only occurred after the optical depth exceeded eight or so. Table 7 also confirms that single forward scattering (*i.e.*, the aerosol diffraction peak) becomes narrower and more

concentrated with increasing particle size. For example, the angular size of the aureole and corona went from being unobservable for haze particles to less than 1.5° for cloud droplets. Although the aureole and corona appeared at relative low optical depths for cloud droplets, the angular extent of these features are outside the FOV considerations of the ABL system.

4. SUMMARY AND POSSIBLE ENHANCEMENTS

4.1 Summary

This analysis has shown that aerosol forward scattering effects are not important for ABL performance and they cannot account for the starlight scintillation reported by Reference 2. The analysis considered possible contributions from the single scattering diffraction peak as well as multiple scattering near the optical axis. Importantly, the characteristic scattering angles for background stratospheric aerosols and thin cirrus are too large, especially when compared with the transmitter divergence angles of the high energy COIL and the tracking laser (on the order of microradians to milliradians). Scattering energy is directed well away from the optical axis and, therefore, the energy received on-axis effectively equals the energy transmitted through the atmosphere. The on-axis forward scattering effects only become important for background stratospheric aerosols and thin cirrus when scattering optical depths of ~ 10 . Even then, it is the reduced transmission of the unscattered beam that make forward scattering effects relatively more important. Thicker cirrus can contain larger particles that could scatter more energy near the optical axis, but the associated optical depths will render the ABL system inoperable in any case.

4.2 Possible Enhancements

Although the above conclusions apply to all scenarios in which ABL will operate, more accurate simulations of the beam spread pattern can be performed. For instance,

1. Instead of a collimated laser beam, consider focusing and adaptive optics of the high energy COIL.
2. Simulate the beam spread pattern for an inhomogeneous scattering medium, such as a finite cloud layer located between the laser and target.

Conceptually, these enhancements can be implemented within the framework of Section 2.3.4. For the assumed Gaussian beam, the expression for W_{vac}^2 (Eq. 18) can be generalized to include beam focusing¹⁹

$$W_{vac}^2 = \frac{z^2}{k^2 W_o^2} + W_o^2 (1 - z/R)^2 \quad (22)$$

¹⁹ Gebhardt, F.G. (1976) High power laser propagation, *Applied Optics*, **15**: 1479-1493.

where R is the focal range. Note that $R \rightarrow \infty$ corresponds to collimated beam propagation and Eq. 22 reduces to Eq. 18.

To accommodate inhomogeneous scattering media, the general procedure is to break the propagation path into a series of homogeneous segments and then evaluate the beam spread at each boundary along the path. For example, assume the transmitter-to-missile path includes a finite cloud layer with vacuum propagation on each side. The beam spread is first evaluated at the near cloud edge using Eqs. 17 and 22. Next, the beam spread is evaluated at the far cloud edge using Eq. 15 where z would be the cloud thickness not the cumulative distance from the transmitter. M_{trans} makes use of $W'_{vac}{}^2$ evaluated at the near cloud edge. Finally, the beam spread is evaluated at the missile distance. To do this, the transmitted and multiple scattering intensities at the far cloud edge are treated separately and then added together. The transmitted component evaluated using Eqs. 17 and 22 and the multiple scattering component is, as a first approach, treated as diffuse radiation.

References

1. W.J. Schafer Associates (Coord.) (1993) *Airborne Laser Workshop on Cirrus and Volcanic Aerosols*, Meeting held at W.J. Schafer Associates, Alexandria, VA.
2. Kramer, M.A. (1993) Stellar Scintillometry Flight aboard HALO," Phillips Laboratory, Albuquerque, NM, PL-TR-93-1004.
3. Herrmann, J. and Zollars, B.G. (1994) "Interpretation of Airborne Stellar Scintillation Measurements Made by the Phillips Laboratory," Massachusetts Institute of Technology Lincoln Laboratory, Lexington, MA, Memo No. 94PM-ACP-030.
4. Harada, L.K., Leslie, D.H., and Salazar, M. (1994) "Atmospheric transmission analysis for airborne laser applications," *Laser Beam Propagation and Control*, from Proceedings SPIE 2120, Los Angeles, CA.
5. Sassen, K. (1991) Corona-producing cirrus cloud properties derived from polarization lidar and photographic analysis, *Applied Optics*, **30**:3421-3428.
6. Bissonnette, L.R. (1988) Multiscattering model for propagation of narrow light beams in aerosol media, *Applied Optics*, **27**: 2478-2484.
7. Mill, J.D. and Shettle, E.P. (1983) "A Preliminary LOWTRAN Snow Model," Air Force Geophysics Laboratory, Hanscom AFB, MA, AFGL-TR-83-1048, ADA129826.
8. Lutomirski, R.L. (1978) Atmospheric degradation of electrooptical system performance, *Applied Optics*, **17**: 3915-3921.
9. Accetta, J.S., and Shumaker, D.L. (Chief Eds.) (1993) *The Infrared and Electro-Optical Systems Handbook, Volume 2, Atmospheric Propagation of Radiation*, F.G. Smith (Ed.), Chapter 1 by M.E. Thomas and D.D. Duncan, ERIM Infrared Information Analysis Center and SPIE Optical Engineering Press (Copubl.), Ann Arbor, Michigan and Bellingham, Washington, p. 123.
10. Grantham, D.D., *et al.* (1985) "Water Vapor, Precipitation, Clouds, and Fog," Chapter 16 in *Handbook of Geophysics and the Space Environment*, A.S. Jursa Scientific Editor, Air Force Geophysics Laboratory, Hanscom AFB, MA, AFGL-TR-85-0315, ADA167000.
11. Sassen, K., Knight, N.C., Takano, Y., and Heymsfield, A.J. (1994) Effects of ice-crystal structure on halo formation: cirrus cloud experimental and ray-tracing modeling studies, *Applied Optics*, **33**:4590-4601.

12. Kneizys, F.X., Shettle, E.P., Abreu, L.W., Chetwynd, J.H., Anderson, G.P., Gallery, W.O., Selby, J.E.A., and Clough, S.A. (1988) *Users Guide to LOWTRAN7*, Air Force Geophysics Laboratory, Hanscom, AFB, Massachusetts, AFGL-TR-88-0177, ADA206773.
13. Koenig, G.G., Longtin, D.R., and Hummel, J.R. (1993) "A Study of the Impact of Cirrus Clouds on High Altitude, Long Horizontal Path Laser Transmission," Phillips Laboratory, Hanscom AFB, MA, PL-TR-93-2263, ADA278563.
14. Accetta, J.S., and Shumaker, D.L. (Chief Eds.) (1993) *The Infrared and Electro-Optical Systems Handbook, Volume 7, Countermeasure Systems*, D. Pollock (Ed.), Chapter 6, *Obscuration Countermeasures* by D.W. Hooch, Jr. and R.A. Sutherland, ERIM Infrared Information Analysis Center and SPIE Optical Engineering Press (Copubl.), Ann Arbor, Michigan and Bellingham, Washington, pp. 412-417.
15. Henyey, L., and Greenstein, J. (1941) Diffuse radiation in the galaxy, *Astrophys. J.*, 93: 70-83.
16. Bohren, C.F. (1991) *What Light Through Yonder Window Breaks?*, John Wiley & Sons, New York, New York, p. 148.
17. Bissonnette, L.R. (1992) Imaging through fog and rain, *Optical Engineering*, 31:1045-1052.
18. Linskens, J.R., and Bohren, C.F. (1994) Appearance of the sun and moon seen through clouds, *Applied Optics*, 21: 4733-4740.
19. Gebhardt, F.G. (1976) High power laser propagation, *Applied Optics*, 15: 1479-1493.

APPENDIX A

Computer Programs Developed in this Effort

A.1 Program *l7abl*

The *l7abl* program calculates aerosol and molecular optical depths and the aerosol phase function for a particular ABL viewing scenario. The code is a simple modification of LOWTRAN7¹² and, thus, it accounts for spherical geometry and atmospheric refraction effects. Currently, *l7abl* operates on a Sun UNIX system.

In *l7abl*, many standard LOWTRAN7 input parameters have been hardwired to reduce the complexity of the *tape5* input file and to force the code to print out the additional ABL information. Table A-1 gives the input format for the *tape5* input file. Users should consult the Users Guide for LOWTRAN7 for additional explanations of the input parameters. Figure A-1 shows a sample input file.

LOWTRAN7's standard output files (*tape6*, *tape7*, and *tape8*) are retained in *l7abl*. Additionally, the code creates an output file named *abl.dat* which contains the information for the ABL viewing scenario. Aerosol and molecular optical depths are printed out layer-by-layer and extend from the ABL altitude to space.

Table A-1. Format of the Input File for *l7abl*. The data are read from *tape5*. Consult the Users Guide for LOWTRAN7 for additional information on the input parameters

RECORD	PARAMETER	UNITS	VALUES
1 (I5)	Model atmosphere	-	1-6 (0 and 7 are disabled)
2 (4I5,F10.3)	Boundary layer aerosol	-	0,1,2,4,5,6 only
	Seasonal aerosol profile	-	0-2
	Profile and type of aerosols above troposphere	-	0-8
	Cloud type	-	0,18,19 only
	Surface visibility	km	>0
2a (3F10.3,I10)	Cirrus thickness	km	≥0
	Cirrus base altitude	km	≥0
	0.55 μm cirrus extinction	km ⁻¹	≥0
	Random number generator	-	≥0
3 (2F10.3)	ABL altitude †	km	>2
	ABL zenith angle	deg	0-100
4 (F10.3)	Laser wavenumber ‡	cm ⁻¹	0-50000

† Viewing conditions should be to space and not intersect the earth

‡ Equals 10000/laser wavelength (μm)

2					
1	0	0	18	0.000	
	0.000	0.000	0.000		0
	9.000	90.000			
	7570.000				

Figure A-1. Sample Input File for *l7abl*. Note that the cirrus parameters for Record 2a are set to 0 which activates default values in LOWTRAN7

A sample output file from *l7abl* is shown in Figure A-2. In Figure A-2, the aerosol optical depths are separated into five columns of data which represent the boundary layer, free troposphere, stratosphere, upper atmosphere and cirrus clouds. For layers with two types of aerosols present, such as stratospheric and cirrus, the aerosol phase functions are weighted according to the scattering optical depths for each component.

A.2 Program *msct*

The *msct* program calculates the multiple small-angle scattering portion of the aerosol modulation transfer function, M_{sct} , as a function of particle separation distance, ρ , and scattering optical depth, τ_{sct} . The governing equations for M_{sct} are Eqs. 5 and 6 of the main text.

The *msct* program reads input data from *abl.dat* which is created by *l7abl* (Section A.1). The code also prompts the user for the beginning and ending layers in *abl.dat* for which values of M_{sct} are to be calculated. The output from *msct* is written to *msct.log*. An example of the output is shown in Figure A-3. Currently, *msct* operates in a DOS environment.

A.3 Program *iradapx*

The *iradapx* program estimates the radius and half-angle spread of a "narrow" beam after it encounters a thin diffuse scattering layer (*i.e.*, a cloud or an aerosol). The scattering layer is located some distance between the transmitter and the target plane. The approximation only considers single scattering. The layer is described by the mean aerosol scattering angle. There is no beam focusing and no beam divergence.

The *iradapx* program is interactive, prompting the user for its input parameters. Three inputs are required:

1. Distance between the transmitter and the diffuse scattering layer (km)
2. Distance between the diffuse scattering layer and the target (km)
3. Mean scattering angle of aerosols in the diffuse scattering layer (deg).

The output from *iradapx* is written to *iradapx.log*. An example of the output is shown in Figure A-4. The half-angle spread is measured with respect to the transmitter. Currently, *iradapx* operates in a DOS environment.

A.4 Program *irad*

The *irad* program calculates the spread of a laser beam in the presence of an aerosol scattering atmosphere. The governing equations are given in Section 2.3.4 of the main text. The effects of atmospheric turbulence, aerosol absorption, and molecular absorption are not included. The aerosol scattering optical depth must be less than 5 and the direction of the aerosol scattering must be predominantly forward. The aerosol phase function $P(\theta)$ is approximated by the Henyey-Greenstein formulation. The transmitter emits a collimated beam with a Gaussian aperture field.

The *irad* program is interactive, prompting the user its inputs. Five input parameters are required:

1. Gaussian aperture intensity radius
2. Laser wavelength
3. Aerosol asymmetry parameter
4. Propagation range
5. Aerosol scattering optical depth over range.

The units and values of input parameters for *irad* are given in Table A-2. The output from *irad* is written to *irad.log*. An example of the output is shown in Figure A-5. The output includes values of $M_{aer}(\rho, \tau_{scl})$, $M_{trans}(\rho)$, and three beam patterns

1. Analytic solution for vacuum propagation
2. FFT solution for vacuum propagation
3. FFT solution including aerosol scattering.

The beam spread patterns are normalized by the (maximum) value along the optical axis for vacuum propagation, and they are expressed in terms of the off-axis angle, $\tan^{-1}(\rho/z)$.

For numerical purposes, the 2-D FFT in Eq. 15 of the main text is replaced by a 1-D FFT so the features of $M_{trans}(\rho)$ and $M_{aer}(\rho, \tau_{scl})$ are, at least, coarsely sampled. That is, the decay of these functions occurs at ρ values that differ by orders of magnitude so a 2-D FFT requires too much computer memory. To help insure proper sampling, *irad* has imposed the limits on the scattering optical depth (≤ 5.0) and Gaussian aperture intensity radius (≤ 0.5 cm). However, if the analytic and FFT beam spread patterns for vacuum propagation (included in the *irad* output) differ significantly or the decay of $M_{aer}(\rho, \tau_{scl})$ occurs entirely at $\rho < 1$ μm , then the sampling is extremely coarse and the resulting beam spreads are gross estimations. Note that the coefficient in Eq. 17 of the main text becomes $\sqrt{P / \pi W_{vac}^2}$ when a 1-D FFT is used. Currently, *irad* operates in a DOS environment.

```

Wavelength (um)
1.3210
Viewing Angle (deg)
90.0000
Aerosol Ext Scaling Factors (B Lay,Trop,Strat,Up AT,Ci
3.214E-01 2.450E-01 1.990E-01 7.301E-01 1.008E+00
Aerosol Abs Scaling Factors (B Lay,Trop,Strat,Up AT,Ci
5.372E-02 2.883E-02 1.284E-04 2.870E-02 1.437E-01
Profiles of Aerosol Scat Coef (km-1) at Wavelength
33
0.000 4.230E-02 0.000E+00 0.000E+00 0.000E+00 0.000E+00
1.000 2.653E-02 0.000E+00 0.000E+00 0.000E+00 0.000E+00
2.000 1.662E-02 0.000E+00 0.000E+00 0.000E+00 0.000E+00
3.000 0.000E+00 7.479E-03 0.000E+00 0.000E+00 0.000E+00
4.000 0.000E+00 3.999E-03 0.000E+00 0.000E+00 0.000E+00
5.000 0.000E+00 2.012E-03 0.000E+00 0.000E+00 0.000E+00
6.000 0.000E+00 1.666E-03 0.000E+00 0.000E+00 0.000E+00
7.000 0.000E+00 1.347E-03 0.000E+00 0.000E+00 0.000E+00
8.000 0.000E+00 7.284E-04 0.000E+00 0.000E+00 0.000E+00
9.000 0.000E+00 3.934E-04 0.000E+00 0.000E+00 0.000E+00
9.950 0.000E+00 2.522E-04 0.000E+00 0.000E+00 0.000E+00
10.050 0.000E+00 0.000E+00 2.227E-04 0.000E+00 1.210E-01
10.950 0.000E+00 0.000E+00 1.617E-04 0.000E+00 1.210E-01
11.050 0.000E+00 0.000E+00 1.572E-04 0.000E+00 0.000E+00
12.000 0.000E+00 0.000E+00 1.275E-04 0.000E+00 0.000E+00
13.000 0.000E+00 0.000E+00 1.028E-04 0.000E+00 0.000E+00
14.000 0.000E+00 0.000E+00 8.790E-05 0.000E+00 0.000E+00
15.000 0.000E+00 0.000E+00 7.855E-05 0.000E+00 0.000E+00
16.000 0.000E+00 0.000E+00 7.597E-05 0.000E+00 0.000E+00
17.000 0.000E+00 0.000E+00 8.452E-05 0.000E+00 0.000E+00
18.000 0.000E+00 0.000E+00 1.034E-04 0.000E+00 0.000E+00
19.000 0.000E+00 0.000E+00 1.155E-04 0.000E+00 0.000E+00
20.000 0.000E+00 0.000E+00 1.171E-04 0.000E+00 0.000E+00
21.000 0.000E+00 0.000E+00 9.983E-05 0.000E+00 0.000E+00
22.000 0.000E+00 0.000E+00 8.353E-05 0.000E+00 0.000E+00
23.000 0.000E+00 0.000E+00 5.966E-05 0.000E+00 0.000E+00
24.000 0.000E+00 0.000E+00 3.938E-05 0.000E+00 0.000E+00
25.000 0.000E+00 0.000E+00 2.605E-05 0.000E+00 0.000E+00
30.000 0.000E+00 0.000E+00 6.602E-06 0.000E+00 0.000E+00
35.000 0.000E+00 0.000E+00 0.000E+00 1.150E-05 0.000E+00
40.000 0.000E+00 0.000E+00 0.000E+00 5.604E-06 0.000E+00
45.000 0.000E+00 0.000E+00 0.000E+00 2.813E-06 0.000E+00
100.000 0.000E+00 0.000E+00 0.000E+00 6.530E-10 0.000E+00
Layer Alts., Drange, Range, Aer Scat Optical Depth at Wavelength
23
9.000 9.950 114.509 114.509 0.000E+00 3.917E-02 0.000E+00 0.000E+00 0.000E+00
9.950 10.050 5.867 120.376 0.000E+00 7.425E-04 6.511E-04 0.000E+00 3.537E-01
10.050 10.950 43.572 163.948 0.000E+00 0.000E+00 8.373E-03 0.000E+00 5.271E+00
10.950 11.050 4.141 168.089 0.000E+00 0.000E+00 6.602E-04 0.000E+00 2.505E-01
11.050 12.000 35.138 203.227 0.000E+00 0.000E+00 4.999E-03 0.000E+00 0.000E+00
12.000 13.000 31.313 234.540 0.000E+00 0.000E+00 3.601E-03 0.000E+00 0.000E+00
13.000 14.000 27.565 262.105 0.000E+00 0.000E+00 2.627E-03 0.000E+00 0.000E+00
14.000 15.000 24.907 287.012 0.000E+00 0.000E+00 2.072E-03 0.000E+00 0.000E+00
15.000 16.000 22.882 309.894 0.000E+00 0.000E+00 1.768E-03 0.000E+00 0.000E+00
16.000 17.000 21.271 331.164 0.000E+00 0.000E+00 1.706E-03 0.000E+00 0.000E+00
17.000 18.000 19.952 351.116 0.000E+00 0.000E+00 1.873E-03 0.000E+00 0.000E+00
18.000 19.000 18.848 369.964 0.000E+00 0.000E+00 2.062E-03 0.000E+00 0.000E+00
19.000 20.000 17.905 387.869 0.000E+00 0.000E+00 2.083E-03 0.000E+00 0.000E+00
20.000 21.000 17.088 404.957 0.000E+00 0.000E+00 1.851E-03 0.000E+00 0.000E+00
21.000 22.000 16.372 421.329 0.000E+00 0.000E+00 1.498E-03 0.000E+00 0.000E+00
22.000 23.000 15.738 437.067 0.000E+00 0.000E+00 1.117E-03 0.000E+00 0.000E+00
23.000 24.000 15.171 452.237 0.000E+00 0.000E+00 7.414E-04 0.000E+00 0.000E+00
24.000 25.000 14.660 466.898 0.000E+00 0.000E+00 4.734E-04 0.000E+00 0.000E+00
25.000 30.000 67.098 533.995 0.000E+00 0.000E+00 9.654E-04 0.000E+00 0.000E+00
30.000 35.000 59.323 593.318 0.000E+00 0.000E+00 1.994E-04 3.350E-04 0.000E+00
35.000 40.000 53.750 647.068 0.000E+00 0.000E+00 0.000E+00 4.432E-04 0.000E+00
40.000 45.000 49.509 696.577 0.000E+00 0.000E+00 0.000E+00 2.013E-04 0.000E+00
45.000 100.000 405.046 1101.623 0.000E+00 0.000E+00 0.000E+00 1.633E-04 0.000E+00

```

Figure A-2. Sample Output File from *l7abl*

```

Layer Alts., Drange, Range, Aer Abs Optical Depth at Wavelength
23
9.000 9.950 114.509 114.509 0.000E+00 5.225E-03 0.000E+00 0.000E+00 0.000E+00
9.950 10.050 5.867 120.376 0.000E+00 9.903E-05 4.205E-07 0.000E+00 5.879E-02
10.050 10.950 43.572 163.948 0.000E+00 0.000E+00 5.408E-06 0.000E+00 8.763E-01
10.950 11.050 4.141 168.089 0.000E+00 0.000E+00 4.264E-07 0.000E+00 4.164E-02
11.050 12.000 35.138 203.227 0.000E+00 0.000E+00 3.229E-06 0.000E+00 0.000E+00
12.000 13.000 31.313 234.540 0.000E+00 0.000E+00 2.326E-06 0.000E+00 0.000E+00

```

13.000	14.000	27.565	262.105	0.000E+00	0.000E+00	1.697E-06	0.000E+00	0.000E+00
14.000	15.000	24.907	287.012	0.000E+00	0.000E+00	1.339E-06	0.000E+00	0.000E+00
15.000	16.000	22.882	309.894	0.000E+00	0.000E+00	1.142E-06	0.000E+00	0.000E+00
16.000	17.000	21.271	331.164	0.000E+00	0.000E+00	1.102E-06	0.000E+00	0.000E+00
17.000	18.000	19.952	351.116	0.000E+00	0.000E+00	1.210E-06	0.000E+00	0.000E+00
18.000	19.000	18.848	369.964	0.000E+00	0.000E+00	1.332E-06	0.000E+00	0.000E+00
19.000	20.000	17.905	387.869	0.000E+00	0.000E+00	1.345E-06	0.000E+00	0.000E+00
20.000	21.000	17.088	404.957	0.000E+00	0.000E+00	1.195E-06	0.000E+00	0.000E+00
21.000	22.000	16.372	421.329	0.000E+00	0.000E+00	9.674E-07	0.000E+00	0.000E+00
22.000	23.000	15.738	437.067	0.000E+00	0.000E+00	7.216E-07	0.000E+00	0.000E+00
23.000	24.000	15.171	452.237	0.000E+00	0.000E+00	4.788E-07	0.000E+00	0.000E+00
24.000	25.000	14.660	466.898	0.000E+00	0.000E+00	3.057E-07	0.000E+00	0.000E+00
25.000	30.000	67.098	533.995	0.000E+00	0.000E+00	6.235E-07	0.000E+00	0.000E+00
30.000	35.000	59.323	593.318	0.000E+00	0.000E+00	1.288E-07	1.371E-05	0.000E+00
35.000	40.000	53.750	647.068	0.000E+00	0.000E+00	0.000E+00	1.814E-05	0.000E+00
40.000	45.000	49.509	696.577	0.000E+00	0.000E+00	0.000E+00	8.239E-06	0.000E+00
45.000	100.000	405.046	1101.623	0.000E+00	0.000E+00	0.000E+00	6.683E-06	0.000E+00
Layer Alts., Drange, Range, Mol Abs Optical Depth at Wavelength								
23								
9.000	9.950	114.509	114.509	2.260E-07				
9.950	10.050	5.867	120.376	5.989E-07				
10.050	10.950	43.572	163.948	2.043E-06				
10.950	11.050	4.141	168.089	7.511E-06				
11.050	12.000	35.138	203.227	2.960E-05				
12.000	13.000	31.313	234.540	1.274E-05				
13.000	14.000	27.565	262.105	1.700E-05				
14.000	15.000	24.907	287.012	2.269E-05				
15.000	16.000	22.882	309.894	3.037E-05				
16.000	17.000	21.271	331.164	4.100E-05				
17.000	18.000	19.952	351.116	5.570E-05				
18.000	19.000	18.848	369.964	7.628E-05				
19.000	20.000	17.905	387.869	1.056E-04				
20.000	21.000	17.088	404.957	1.474E-04				
21.000	22.000	16.372	421.329	2.078E-04				
22.000	23.000	15.738	437.067	3.108E-04				
23.000	24.000	15.171	452.237	5.075E-04				
24.000	25.000	14.660	466.898	1.131E-03				
25.000	30.000	67.098	533.995	3.751E-03				
30.000	35.000	59.323	593.318	7.966E-04				
35.000	40.000	53.750	647.068	1.637E-02				
40.000	45.000	49.509	696.577	3.734E-03				
45.000	100.000	405.046	1101.623	2.242E-01				

Figure A-2. (cont.) Sample Output File from *l7abl*

Normalized Aer Phase Function (0-180 deg) at Wavelength

23

9.000	9.950	6.513E-01	6.478E-01	6.375E-01	6.209E-01	5.990E-01	5.726E-01	5.430E-01
9.000	9.950	4.784E-01	4.126E-01	3.511E-01	2.964E-01	2.495E-01	2.101E-01	1.774E-01
9.000	9.950	1.190E-01	8.303E-02	6.043E-02	4.577E-02	3.597E-02	2.922E-02	2.448E-02
9.000	9.950	2.109E-02	1.977E-02	1.865E-02	1.770E-02	1.689E-02	1.622E-02	1.566E-02
9.000	9.950	1.521E-02	1.485E-02	1.458E-02	1.439E-02	1.427E-02	1.424E-02	
9.950	10.050	2.065E+01	1.671E+01	1.015E+01	5.686E+00	3.264E+00	1.977E+00	1.266E+00
9.950	10.050	5.965E-01	3.238E-01	1.945E-01	1.260E-01	8.637E-02	6.194E-02	4.605E-02
9.950	10.050	2.475E-02	1.506E-02	1.002E-02	7.134E-03	5.367E-03	4.229E-03	3.467E-03
9.950	10.050	2.944E-03	2.745E-03	2.579E-03	2.441E-03	2.326E-03	2.230E-03	2.152E-03
9.950	10.050	2.089E-03	2.040E-03	2.004E-03	1.978E-03	1.963E-03	1.958E-03	
10.050	10.950	2.070E+01	1.675E+01	1.017E+01	5.698E+00	3.271E+00	1.981E+00	1.268E+00
10.050	10.950	5.970E-01	3.238E-01	1.943E-01	1.256E-01	8.599E-02	6.158E-02	4.572E-02
10.050	10.950	2.450E-02	1.488E-02	9.891E-03	7.042E-03	5.297E-03	4.171E-03	3.416E-03
10.050	10.950	2.896E-03	2.698E-03	2.532E-03	2.392E-03	2.276E-03	2.180E-03	2.100E-03
10.050	10.950	2.036E-03	1.986E-03	1.948E-03	1.921E-03	1.906E-03	1.901E-03	
10.950	11.050	2.068E+01	1.673E+01	1.016E+01	5.693E+00	3.268E+00	1.979E+00	1.267E+00
10.950	11.050	5.968E-01	3.238E-01	1.944E-01	1.258E-01	8.616E-02	6.174E-02	4.587E-02
10.950	11.050	2.461E-02	1.496E-02	9.948E-03	7.083E-03	5.328E-03	4.197E-03	3.439E-03
10.950	11.050	2.917E-03	2.719E-03	2.553E-03	2.414E-03	2.298E-03	2.202E-03	2.123E-03
10.950	11.050	2.060E-03	2.010E-03	1.973E-03	1.947E-03	1.931E-03	1.926E-03	
11.050	12.000	4.797E-01	4.778E-01	4.721E-01	4.632E-01	4.516E-01	4.378E-01	4.224E-01
11.050	12.000	3.882E-01	3.518E-01	3.152E-01	2.797E-01	2.464E-01	2.157E-01	1.879E-01
11.050	12.000	1.313E-01	9.120E-02	6.403E-02	4.633E-02	3.525E-02	2.864E-02	2.502E-02
11.050	12.000	2.336E-02	2.304E-02	2.298E-02	2.311E-02	2.339E-02	2.377E-02	2.423E-02
11.050	12.000	2.474E-02	2.524E-02	2.571E-02	2.612E-02	2.640E-02	2.650E-02	
12.000	13.000	4.797E-01	4.778E-01	4.721E-01	4.632E-01	4.516E-01	4.378E-01	4.224E-01
12.000	13.000	3.882E-01	3.518E-01	3.152E-01	2.797E-01	2.464E-01	2.157E-01	1.879E-01
12.000	13.000	1.313E-01	9.120E-02	6.403E-02	4.633E-02	3.525E-02	2.864E-02	2.502E-02
12.000	13.000	2.336E-02	2.304E-02	2.298E-02	2.311E-02	2.339E-02	2.377E-02	2.423E-02
12.000	13.000	2.474E-02	2.524E-02	2.571E-02	2.612E-02	2.640E-02	2.650E-02	
13.000	14.000	4.797E-01	4.778E-01	4.721E-01	4.632E-01	4.516E-01	4.378E-01	4.224E-01
13.000	14.000	3.882E-01	3.518E-01	3.152E-01	2.797E-01	2.464E-01	2.157E-01	1.879E-01
13.000	14.000	1.313E-01	9.120E-02	6.403E-02	4.633E-02	3.525E-02	2.864E-02	2.502E-02
13.000	14.000	2.336E-02	2.304E-02	2.298E-02	2.311E-02	2.339E-02	2.377E-02	2.423E-02
13.000	14.000	2.474E-02	2.524E-02	2.571E-02	2.612E-02	2.640E-02	2.650E-02	
14.000	15.000	4.797E-01	4.778E-01	4.721E-01	4.632E-01	4.516E-01	4.378E-01	4.224E-01
14.000	15.000	3.882E-01	3.518E-01	3.152E-01	2.797E-01	2.464E-01	2.157E-01	1.879E-01
14.000	15.000	1.313E-01	9.120E-02	6.403E-02	4.633E-02	3.525E-02	2.864E-02	2.502E-02
14.000	15.000	2.336E-02	2.304E-02	2.298E-02	2.311E-02	2.339E-02	2.377E-02	2.423E-02
14.000	15.000	2.474E-02	2.524E-02	2.571E-02	2.612E-02	2.640E-02	2.650E-02	
15.000	16.000	4.797E-01	4.778E-01	4.721E-01	4.632E-01	4.516E-01	4.378E-01	4.224E-01
15.000	16.000	3.882E-01	3.518E-01	3.152E-01	2.797E-01	2.464E-01	2.157E-01	1.879E-01
15.000	16.000	1.313E-01	9.120E-02	6.403E-02	4.633E-02	3.525E-02	2.864E-02	2.502E-02
15.000	16.000	2.336E-02	2.304E-02	2.298E-02	2.311E-02	2.339E-02	2.377E-02	2.423E-02
15.000	16.000	2.474E-02	2.524E-02	2.571E-02	2.612E-02	2.640E-02	2.650E-02	
16.000	17.000	4.797E-01	4.778E-01	4.721E-01	4.632E-01	4.516E-01	4.378E-01	4.224E-01
16.000	17.000	3.882E-01	3.518E-01	3.152E-01	2.797E-01	2.464E-01	2.157E-01	1.879E-01
16.000	17.000	1.313E-01	9.120E-02	6.403E-02	4.633E-02	3.525E-02	2.864E-02	2.502E-02
16.000	17.000	2.336E-02	2.304E-02	2.298E-02	2.311E-02	2.339E-02	2.377E-02	2.423E-02
16.000	17.000	2.474E-02	2.524E-02	2.571E-02	2.612E-02	2.640E-02	2.650E-02	
...
...
...
40.000	45.000	3.357E+00	2.770E+00	2.205E+00	1.772E+00	1.440E+00	1.182E+00	9.808E-01
40.000	45.000	6.973E-01	5.137E-01	3.886E-01	2.999E-01	2.347E-01	1.855E-01	1.479E-01
40.000	45.000	8.680E-02	5.339E-02	3.443E-02	2.340E-02	1.689E-02	1.308E-02	1.097E-02
40.000	45.000	1.015E-02	1.022E-02	1.062E-02	1.145E-02	1.289E-02	1.512E-02	1.829E-02
40.000	45.000	2.228E-02	2.580E-02	2.615E-02	2.523E-02	2.990E-02	3.617E-02	
45.000	100.000	3.357E+00	2.770E+00	2.205E+00	1.772E+00	1.440E+00	1.182E+00	9.808E-01
45.000	100.000	6.973E-01	5.137E-01	3.886E-01	2.999E-01	2.347E-01	1.855E-01	1.479E-01
45.000	100.000	8.680E-02	5.339E-02	3.443E-02	2.340E-02	1.689E-02	1.308E-02	1.097E-02
45.000	100.000	1.015E-02	1.022E-02	1.062E-02	1.145E-02	1.289E-02	1.512E-02	1.829E-02
45.000	100.000	2.228E-02	2.580E-02	2.615E-02	2.523E-02	2.990E-02	3.617E-02	

Figure A-2. (cont.) Sample Output File from *l7abl*

```

Aer abs optical depth over path: 0.0000E+00
Aer abs MCF over path:          1.0000E+00
Mol abs optical depth over path: 0.0000E+00
Mol abs MCF over path:          1.0000E+00

```

```

Layer #, Layer & Cum Path length (km):      1      1.0000      1.0000
Aer sct optical depth over layer:            1.0000E+00
Integrated Phase Function (should be 1.0):  1.0088
Aerosol RMS Scattering Angle (deg):         51.6477

```

RHO(UM)	FRHO	MCF
.000	1.0000	1.0000
.010	.9996	.9994
.013	.9994	.9990
.016	.9990	.9985
.020	.9985	.9976
.025	.9976	.9962
.032	.9962	.9940
.040	.9940	.9905
.050	.9905	.9851
.063	.9851	.9765
.079	.9765	.9632
.100	.9631	.9427
.126	.9425	.9116
.158	.9113	.8658
.200	.8653	.8006
.251	.8000	.7133
.316	.7135	.6059
.398	.6098	.4889
.501	.5032	.3806
.631	.4121	.2968
.794	.3395	.2353
1.000	.2714	.1815
1.259	.2167	.1408
1.585	.1725	.1096
1.995	.1379	.0861
2.512	.1096	.0674
3.162	.0869	.0528
3.981	.0689	.0415
5.012	.0547	.0327
6.310	.0436	.0259
7.943	.0346	.0205
10.000	.0274	.0162
12.589	.0218	.0128
15.849	.0173	.0102
19.953	.0138	.0081
25.119	.0109	.0064
31.623	.0087	.0051
39.811	.0069	.0040
50.119	.0055	.0032
63.096	.0059	.0034
79.433	.0054	.0031
100.000	.0049	.0029
125.893	.0052	.0030
158.489	.0049	.0028
199.526	.0050	.0029

Figure A-3. Sample Output File from *msct*

```

Layer #, Layer & Cum Path length (km):      2      1.0000      2.0000
Aer sct optical depth over layer:           1.0000E+00
Integrated Phase Function (should be 1.0):  1.0187
Aerosol RMS Scattering Angle (deg):         30.1871

```

RHO(UM)	FRHO	MCF
.000	1.0000	1.0000
.010	.9998	.9998
.013	.9998	.9996
.016	.9996	.9994
.020	.9994	.9990
.025	.9990	.9985
.032	.9985	.9976
.040	.9976	.9962
.050	.9962	.9941
.063	.9941	.9906
.079	.9906	.9853
.100	.9853	.9769
.126	.9771	.9641
.158	.9645	.9448
.200	.9457	.9163
.251	.9185	.8762
.316	.8813	.8229
.398	.8339	.7579
.501	.7790	.6863
.631	.7206	.6143
.794	.6580	.5418
1.000	.5873	.4650
1.259	.5140	.3910
1.585	.4402	.3218
1.995	.3695	.2602
2.512	.3042	.2069
3.162	.2464	.1626
3.981	.1973	.1269
5.012	.1572	.0991
6.310	.1250	.0775
7.943	.0993	.0607
10.000	.0788	.0477
12.589	.0626	.0376
15.849	.0497	.0297
19.953	.0395	.0235
25.119	.0314	.0186
31.623	.0249	.0147
39.811	.0198	.0116
50.119	.0157	.0092
63.096	.0130	.0076
79.433	.0105	.0062
100.000	.0086	.0050
125.893	.0074	.0043
158.489	.0063	.0037
199.526	.0057	.0034

Figure A-3. (cont.) Sample Output File from *msct*

Distance from Transmitter-to-Layer:	50.000 km	
Distance from Layer-to-Target:	50.000 km	
Mean Scattering Angle for Layer:	30.200 deg	
Half-Angle Spread of the Beam:	16.225 deg	283.186 mrad
Radius of the Beam:	29.101 km	

Figure A-4. Sample Output File from *iradapx*

Table A-2. Input Parameters for *irad*. The parameters are entered interactively by the user

INPUT PARAMETER	UNITS	VALUES
Gaussian aperture intensity radius	cm	>0.0 and ≤0.5
Laser wavelength	μm	0.2-40.0
Aerosol asymmetry parameter [†]	-	≥0.7 and <1.0
Propagation range	km	>0.0
Aerosol scattering optical depth over range	-	≥0.0 and ≤5.0

[†] Used to evaluate the Henyey-Greenstein phase function

```

Gaussian Beam Width, W0:          1.00E-01 cm
Laser Wavelength:                  .55 um
Aerosol Asymmetry Parameter:       .70
Propagation Range:                 1.00E+00 km
Aerosol Scattering Optical Depth over Range: 5.00E+00
Integrated Phase Function (should be 1.0): 1.0000
Mean Squared Scattering Angle (rad sq): 7.5625E-01

```

Aerosol MCF		
RHO (MM)	FRHO	MCF
.0000000	1.0000	1.0000
.0000100	.9996	.9982
.0000126	.9994	.9971
.0000158	.9991	.9954
.0000200	.9985	.9927
.0000251	.9977	.9884
.0000316	.9963	.9817
.0000398	.9942	.9713
.0000501	.9908	.9550
.0000631	.9855	.9299
.0000794	.9771	.8919
.0001000	.9641	.8358
.0001259	.9442	.7564
.0001585	.9140	.6504
.0001995	.8695	.5208
.0002512	.8069	.3808
.0003162	.7245	.2523
.0003981	.6270	.1549
.0005012	.5280	.0944
.0006310	.4433	.0618
.0007943	.3713	.0431
.0010000	.2987	.0300
.0012589	.2402	.0224
.0015849	.1909	.0175
.0019953	.1526	.0145
.0025119	.1213	.0124
.0031623	.0961	.0109
.0039811	.0763	.0099
...
...
...
15.8489300	.0100	.0071
19.9526200	.0100	.0071
25.1188700	.0099	.0071
31.6227800	.0100	.0071
39.8107200	.0100	.0071
50.1187200	.0100	.0071
63.0957300	.0100	.0071

Figure A-5. Sample Output File from *irad*

Aperture MTF	
RHO (MM)	MTF
.000	1.0000
.100	.9975
.200	.9900
.300	.9778
.400	.9608
.500	.9394
.600	.9139
.700	.8847
.800	.8521
.900	.8167
1.000	.7788
1.100	.7390
1.200	.6977
1.300	.6554
1.400	.6126
1.500	.5698
1.600	.5273
1.700	.4855
1.800	.4449
1.900	.4056
2.000	.3679
2.100	.3320
2.200	.2982
2.300	.2665
2.400	.2369
2.500	.2096
2.600	.1845
2.700	.1616
2.800	.1409
2.900	.1222
3.000	.1054
3.100	.0905
3.200	.0773
3.300	.0657
3.400	.0556
3.500	.0468
3.600	.0392
3.700	.0326
3.800	.0271
3.900	.0223
4.000	.0183
4.100	.0150
4.200	.0122
4.300	.0098
4.400	.0079
4.500	.0063
...	...
...	...
...	...
16.100	.0000
16.200	.0000
16.300	.0000

Figure A-5. (cont.) Sample Output File from *irad*

THET (MRAD)	Irradiance Field		
	VAC ANAL	VAC FFT	ATM MTF
0.0000E+00	1.0000E+00	1.0001E+00	7.3918E-03
1.6785E-02	9.6390E-01	9.6396E-01	7.1362E-03
3.3569E-02	8.6325E-01	8.6329E-01	6.4232E-03
5.0354E-02	7.1831E-01	7.1832E-01	5.3965E-03
6.7139E-02	5.5533E-01	5.5533E-01	4.2421E-03
8.3923E-02	3.9889E-01	3.9888E-01	3.1341E-03
1.0071E-01	2.6621E-01	2.6618E-01	2.1944E-03
1.1749E-01	1.6508E-01	1.6505E-01	1.4781E-03
1.3428E-01	9.5104E-02	9.5080E-02	9.8250E-04
1.5106E-01	5.0907E-02	5.0890E-02	6.6946E-04
1.6785E-01	2.5318E-02	2.5307E-02	4.8817E-04
1.8463E-01	1.1699E-02	1.1693E-02	3.9164E-04
2.0142E-01	5.0228E-03	5.0197E-03	3.4428E-04
2.1820E-01	2.0036E-03	2.0021E-03	3.2282E-04
2.3499E-01	7.4254E-04	7.4189E-04	3.1384E-04
2.5177E-01	2.5569E-04	2.5543E-04	3.1036E-04
2.6855E-01	8.1806E-05	8.1712E-05	3.0911E-04
2.8534E-01	2.4317E-05	2.4250E-05	3.0871E-04
3.0212E-01	6.7160E-06	6.6791E-06	3.0860E-04
3.1891E-01	1.7234E-06	1.6962E-06	3.0858E-04
3.3569E-01	4.1089E-07	3.9774E-07	3.0859E-04
3.5248E-01	9.1020E-08	7.3356E-08	3.0860E-04
3.6926E-01	1.8733E-08	8.0543E-09	3.0862E-04
3.8605E-01	3.5822E-09	1.5516E-08	3.0863E-04
4.0283E-01	6.3646E-10	1.5516E-08	3.0864E-04
4.1962E-01	1.0506E-10	1.5516E-08	3.0866E-04
4.3640E-01	1.6114E-11	1.5516E-08	3.0868E-04
4.5319E-01	2.2962E-12	1.5516E-08	3.0871E-04
4.6997E-01	3.0402E-13	1.5516E-08	3.0873E-04
4.8676E-01	3.7399E-14	1.5516E-08	3.0876E-04
5.0354E-01	4.2746E-15	1.5516E-08	3.0877E-04
5.2032E-01	4.5391E-16	1.5516E-08	3.0878E-04
5.3711E-01	4.4786E-17	1.5516E-08	3.0878E-04
5.5389E-01	4.1056E-18	1.5516E-08	3.0877E-04
5.7068E-01	3.4967E-19	1.5516E-08	3.0874E-04
5.8746E-01	2.7672E-20	1.5516E-08	3.0871E-04
6.0425E-01	2.0346E-21	1.5516E-08	3.0867E-04
6.2103E-01	1.3899E-22	1.5516E-08	3.0863E-04
6.3782E-01	8.8218E-24	1.5516E-08	3.0858E-04
6.5460E-01	5.2023E-25	1.5516E-08	3.0854E-04
6.7139E-01	2.8503E-26	1.5516E-08	3.0849E-04
6.8817E-01	1.4511E-27	1.5516E-08	3.0844E-04
7.0496E-01	6.8633E-29	1.5516E-08	3.0840E-04
7.2174E-01	3.0162E-30	1.5516E-08	3.0836E-04
7.3853E-01	1.2315E-31	1.5516E-08	3.0833E-04
...
...
...
2.6752E+02	0.0000E+00	7.0707E-11	2.6987E-04
2.6768E+02	0.0000E+00	1.5516E-08	2.6987E-04
2.6784E+02	0.0000E+00	8.5778E-10	2.6987E-04
2.6799E+02	0.0000E+00	5.0231E-10	2.6987E-04
2.6815E+02	0.0000E+00	1.5516E-08	2.6987E-04
2.6830E+02	0.0000E+00	1.5516E-08	2.6987E-04

Figure A-5. (cont.) Sample Output File from *irad*. Shortened for brevity